2015

New nanostructured alloy and metal sulfide materials for sodium-ion batteries

Kan Huang
University of Wollongong

Institute for Superconducting and Electronic Materials,

Faculty of Engineering

New Nanostructured Alloy and Metal Sulfide Materials for Sodium-ion Batteries

From

UNIVERSITY OF WOLLONGONG

BY KAN HUANG, B. Sc.

"A thesis submitted in fulfillment of the requirements for the award of the degree of

Master of Engineering - Research

at the University of Wollonggong"

2015

CERTIFICATION

I, Kan Huang, declare that this thesis, submitted in fulfillment of the requirements for the award of Master of Engineering by Research, in the Institute for Superconducting & Electronic Materials, Faculty of Engineering, University of Wollongong, is totally my own work unless otherwise referenced or acknowledged. This document has not been submitted for qualifications at any other academic institution.

Kan Huang

20 August, 2014

DEDICATION

For my beloved grandfather, grandmother, father, mother, and friends, who have loved and supported me all my life.

ACKNOWLEDGEMENTS

Firstly, I would like to express my heartfelt appreciation to my supervisor, Prof. Zaiping Guo for her rich academic knowledge, guidance, and supervision, financial support of my experiments, and constant encouragement and suggestions during my one and a half years' research study at the University of Wollongong.

Also, I would like to thank Prof. Shi Xue Dou and Prof. Hua Kun Liu for their meaningful comments and suggestions, as well as for providing appropriate facilities for my research work.

I want to thank all the staff, especially for the technical support from the staff members at the University of Wollongong, such as Dr. Kosta Konstantinov (TGA/DTA) Mr. Darren Attard (SEM/EDX, FE-SEM), Dr. Germanas Peleckis (XRD), Dr. Zhixin Chen, and Dr. David Wexler (TEM), and all the other laboratory supervisors are gratefully acknowledged. Special thanks go to Dr.Tania Silver, for her careful editing of manuscripts and of this thesis.

I am also very grateful to Dr. Tengfei Zhou for his unselfish help on my research work and patient guidance in experimental methods and measurements during my Master's degree's study. Moreover, I wish to thank Ms. Sha Li, Dr. Kuok Hao Seng, Ms. Dan Li, Mr. Hongqiang Wang, Ms. Li Li, Mr. Jincheng Zhuang, Mr. Sujith Kalluri, Mr. Mohammad Ihsan, Mr. Jun Wang, Dr. Qi Li, Mr. Chao Han, Mr. Weijie Li, Mr. Zhixin Tai and other members of ISEM.

Finally, I would like to express my deep appreciation and love to my family, including my father, my sisters, my brothers, my nephew, and my niece for their love, understanding, and support.

ABSTRACT

Lithium (Li)-ion batteries have attracted wide attention for grid-scale energy storage application in the last several years. The price of lithium-ion batteries is dramatically constrained, however, by the extent of lithium sources. Therefore, sodium-ion batteries are regarded as a substitute for lithium-ion batteries because of both the low cost associated with the high natural abundance of sodium and the decent energy densities, which is similar to those for Li. This Master's work on sodium-ion batteries can be mainly divided into two parts: 1) synthesis of antimony-tin alloy materials for anode materials in sodium-ion batteries; 2) synthesis and characterization of carbon-coated Graphene-SnO_2 (i.e., Gr-SnO_2-C), carbon-coated Graphene-SnS (Gr-SnS-C) as anode materials for rechargeable sodium-ion batteries.

Alloy-based materials were prepared by a simple and low-cost technique with the addition of a reducing reagent. Firstly, polyacrylonitrile (PAN) was first dissolved into N,N-dimethylformamide(DMF). Then, antimony chloride and tin chloride dihydrate were added to the solution, followed by a simple electrospinning method. After carbonization, SnSb alloy could be obtained. By this method, nanofibers with a diameter of 100nm nanofiber could be obtained, which creates pathways for ion conduction. At the same time, numerous factors that have an impact on performance and many comparisons were investigated, for example, the selection of different binders, different electrolytes, etc. SnSb alloy shows a relatively higher electrochemical performance than pure Sb and pure Sn. In terms of the selection of binders, carboxymethyl cellulose (CMC) binders have higher performance than PVDF. What is more, the composites which contain PAN also provide higher capacity and better rate capability. After several comparisons, SnSb nanofiber which uses CMC as binder and PAN in its solution was found to have the best electrochemical performance (480mAh g^{-1} after 100cycles) with the current density of 270mA g^{-1}. The excellent electrochemical performance indicates that the SnSb alloy nanofiber could be a very promising candidate as anode material for sodium-ion batteries.

For carbon coated Graphene-SnS (Gr-SnS), firstly, Graphene-SnO_2 (Gr-SnO_2) material was prepared by an environmentally friendly and simple hydrothermal technique. Then, carbon-coated SnO_2/graphene nanosheets (Gr-SnO_2-C) were also synthesized on the gram scale via a similar hydrothermal method, followed by carbonization. In this method, the obtained SnO_2 particles are uniformly distributed on the surface of the graphene and the carbon coating layer, which can work together to effectively maintain the stability of the structural arrangement, serve as good electronic conductors, and allows Na^+ access. In addition, the surface carbon coating layer can effectively separate the SnO_2/graphene sheets, preventing aggregation during the charge/discharge processes. After sulfidation, the Gr-SnO_2-C was transformed to carbon-coated Graphene-SnS (Gr-SnS-C). The composite provides quite good electrochemical performance, 680mAh g^{-1} at the current density of 90mAg^{-1}. This work reveals a new method to prepare carbon-coated metal oxide on graphene, which could be used to prepare electrode materials with excellent electrochemical performance for sodium-ion batteries.

TABLE OF CONTENTS

LIST OF FIGURES

LIST OF TABLES

CHAPTER 1 INTRODUCTION

Recently, lithium (Li)-ion batteries have attracted wide attentions for grid-scale energy storage application in the last several years.[1] Their high cost, low stability, and safety issues could be the main barriers, however, for their wide usage. As an alternative to the Li-ion batteries, the Na-ion battery (SIB) has recently again attracted considerable attention for large-scale energy storage in renewable energy and smart grid applications, because of both the low cost associated with the high natural abundance of sodium and the decent energy densities, which are similar to those for Li.[2-5] Given this similarity, many mature electrode materials for the Li-ion chemistry have been investigated as drop-in replacements for Na-ion batteries.[6] Great efforts had been made on sodium ion batteries using this tactic, but without good performance, simply because the Na ions have a larger radius than Li ions, which triggers difficulties for rapid ion insertion and extraction, leading to poor cycling stability and low capacity.[7] Only a few candidates are capable of reversible insertion/extraction for Na ions.

In the field of sodium-ion batteries, there are many research areas and many methods to enhance performance, such as synthesizing new anode and cathode materials for electrodes with high capacity or creating different nanostructured materials. In this study, nanostructured electrode materials with different morphology and particular structures, such as mesoporous, shell, and nanofiber structures, have been synthesised to achieve better electrochemical performance for sodium-ion batteries.

Chapter 2 presents a systematic review of lithium batteries and sodium batteries, including the basic concepts of batteries (rechargeable batteries, lithium-ion batteries, and sodium-ion batteries), the history of battery development, and a review of the recent literature on SIBs.

Chapter 3 describes all the experimental methods and chemicals used in this study in detail. The fabrication procedures and techniques used for synthesizing the electrode materials are also mentioned specifically.

Chapter 4 presents a series of impact factors that were investigated, such as the choice of electrolyte, the choice of binder, and the choice of solution. From many comparisons, the best choice of conditions can be selected for better electrochemical performance. It also describes the facile synthesis of nanofibers which encapsulated tin-antimony alloy, by a very simple electrospinning method. High capacity and good stability were achieved for SnSb alloy anode in sodium-ion batteries

Chapter 5 reports the synthesis and characterization of carbon-coated graphene-SnS composites with a special yolk-shell structure as anode material for sodium-ion batteries. As the result of a two-step hydrothermal method, the graphene-tin/antimony-carbon (Gr-SnS-C) composite, which contains both a carbon and a graphene layer, could deliver much higher capacity and maintain good cycling stability.

Chapter 6 summarizes the general conclusions of this study

CHAPTER 2 LITERATURE REVIEW

2. 1 Introduction to Sodium-ion Batteries

2.1.1 General introduction to sodium-ion batteries.

With the development of the global economy and modern technology, the energy supply plays a dominant role in our daily lives, which has generated the need for rechargeable batteries with both high energy density and high rate capability. Lithium-ion batteries show outstanding electrochemical performance among all the different rechargeable battery systems, as shown in Figure 2.1.[8]

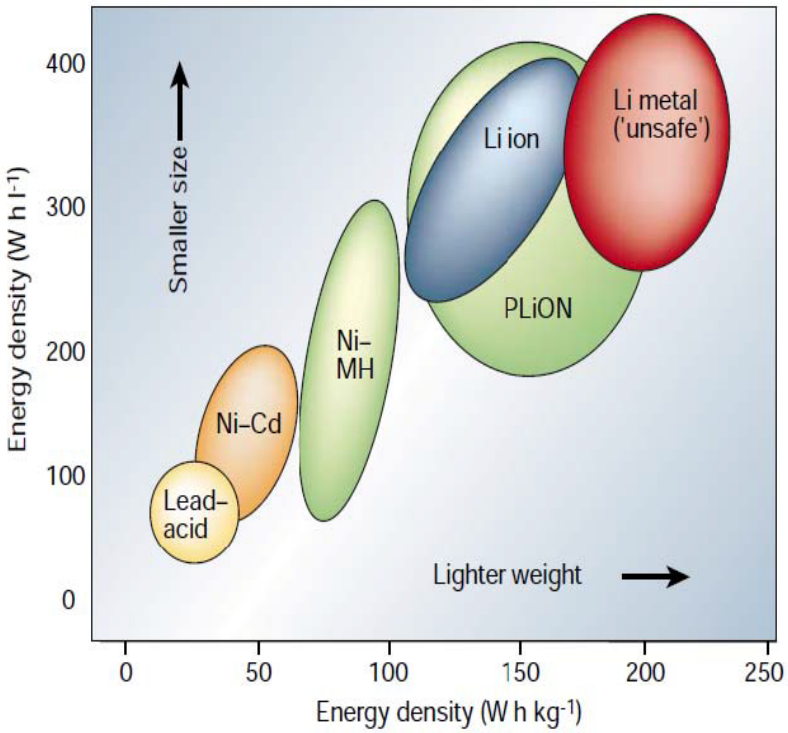

Figure 2.1 Comparison of the different battery technologies in terms of volumetric and gravimetric energy density.[8]

As shown in Figure 2.2, the use of lithium-ion batteries has expanded rapidly and will continue to increase, which will dramatically increase the price of Li-ion batteries because of the relatively low natural abundance of lithium.[9] Due to the abundance of sodium, its low price, greater safety, and the high similarity of both Li and Na insertion systems, sodium-ion batteries are attracting more and more attention as the replacement for Li-ion batteries.[10]

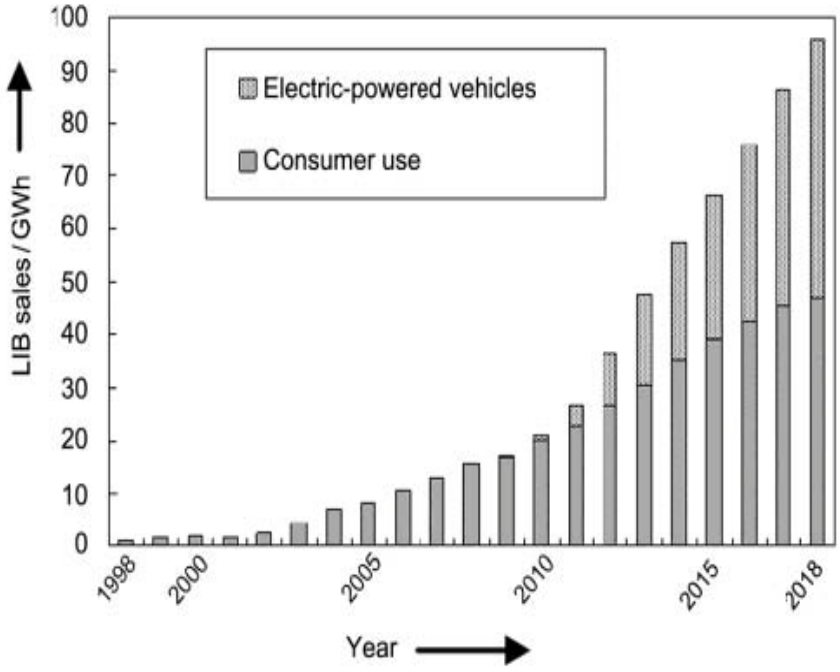

Figure 2.2 Forecast expansion in demand for lithium-ion batteries. GWh = gigawatt hours.[9]

The sodium-ion battery was first researched in the late 1970s along with the research on lithium-ion batteries.[11] It did not receive much attention at first, mainly because of the excellent performance of Li-ion batteries. While the lithium-ion battery technology is quite mature, there are still many problems which cannot be solved, such as lifetime, safety, poor performance at low temperature, and low abundance of Li, leading to the rapid development of research on the sodium-ion battery. According to Table 2.1, it can be seen that Li is much more expensive than Na.[12] Therefore, great efforts have been made in this area in order to

catch up with Li-ion technology, mainly in two directions, finding new materials which have good electrochemical performance and synthesizing new nanostructures.

Metal	Atonic weight/(g/mol)	Voltage/V	Price/t	Radium/Å	Abundance/%
Li	6.94	-3.043862	5000	0.69	0.00006
Na	22.99	-2.711166	150	0.98	0.0264

Table 2.1 Lithium versus Sodium characteristics.[12]

2.1.2 Basic mechanism of sodium-ion batteries

In order to supply the needed voltage and enough capacity, a battery is often composed of several cells, each of which include three main parts, a positive electrode (cathode), a negative electrode (anode), and an appropriate electrolyte. The main reactions are the transfer of sodium ions from the cathode to anode and back again through the electrolyte. The principle of the sodium-ion battery is shown in Figure 2.3.

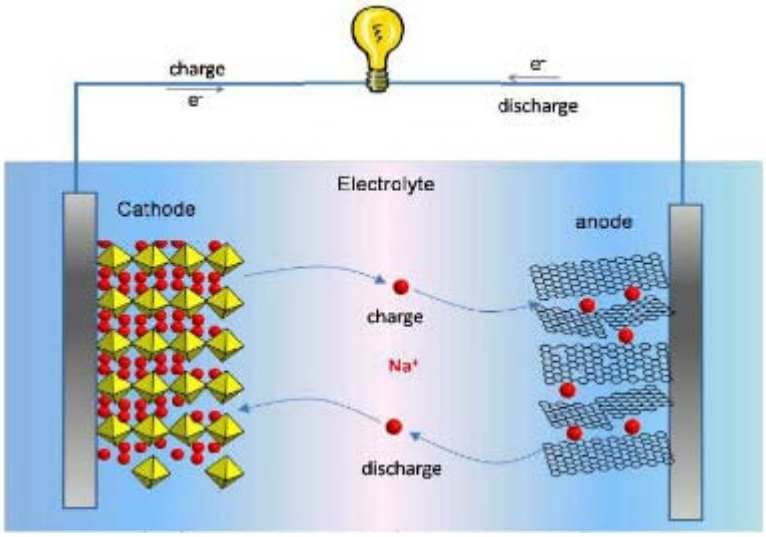

Figure 2.3 Schematic of diagram Na^+ extraction and insertion in rechargeable sodium-ion batteries.

In sodium-ion batteries, when the battery is discharged, Na^+ ions are transferred from the anode and then inserted into the cathode through the electrolyte. When the battery is charged, the process is reversed.

2.1.3 Basic concepts and principles

As mentioned above, a battery is often composed of several cells, which each include three main parts, a positive electrode (cathode), a negative electrode (anode), and an appropriate electrolyte. What is more, there is a separator between half cells allowing ions to flow and preventing contact between different electrolytes. During the discharge process, reduction occurs at the cathode, which leads to the acquisition of electrons, while oxidation occurs at anode, which deprives it of electrons. To better analyze the electrochemical performance and describe the battery system, some basic concepts and principles should be discussed as follows:

(a) Potential

A standard cell potential can be determined by the potential difference between the anode and cathode of the sodium-ion battery.

$$\Delta G = -EF \tag{2.1}$$

where ΔG = Gibbs free energy

F= Faraday constant (96485.3399C mol^{-1})

E = Electrode potential

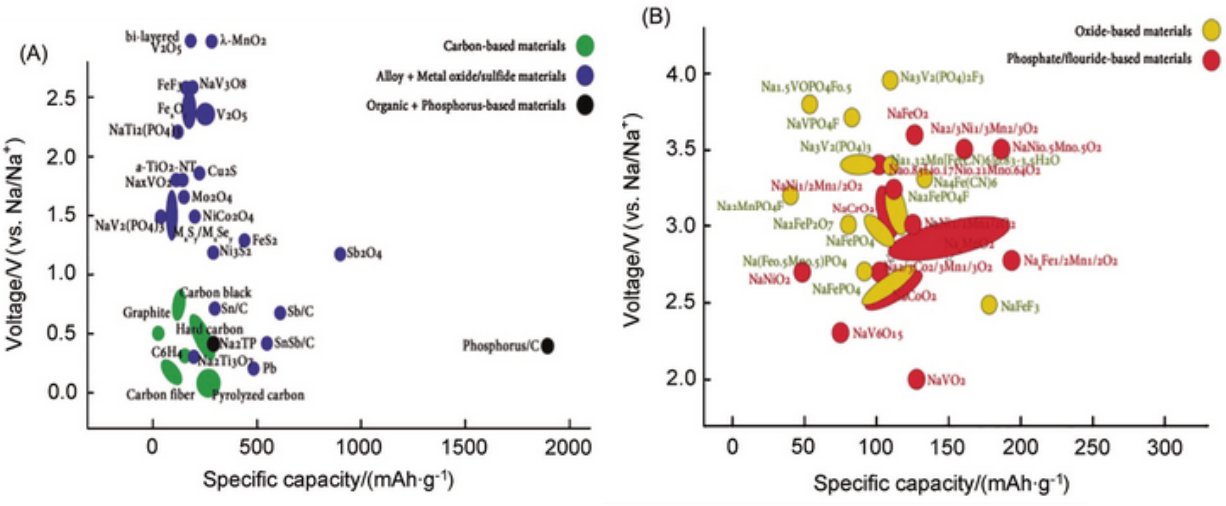

Figure 2.4 Voltage versus capacity for anode (A) and cathode (B) materials. The output voltage values for Na-ion cells or Na-metal cells are represented.[13]

For sodium rechargeable batteries, most of the cathode and anode materials are represented in Figure 2.4, in which the electrochemical potential and the typical sodium ion storage capacities of both anodic and cathodic materials are summarized.[13] The terms 'cathode' and 'anode' are defined in terms of the higher or lower potential electrode, respectively. Therefore, the active materials discussed later will all be acting as cathode (with Na metal anode) in a half cell, but actually, what they really are is determined by their potentials.

(b) Open circuit voltage (OCV)

Open circuit voltage is the voltage across the terminals of a cell or battery when no external current flows. It is usually close to the thermodynamic voltage for the system.

(c) Discharging

Discharging is the operation which batteries deliver electrical energy to an external load.

(d) Charging

Charging is the operation in which the battery is restored to its original charged condition by reversal of the current flow.

(e) Theoretical specific capacity

The theoretical capacity is a significant parameter used to evaluate the performance of active materials. The theoretical capacity (Q_{TSC}) can be calculated by the following equation:

$$Q_{TSC} = \frac{n \times F}{M} \quad (2.2)$$

Where *n* is the number of moles of electrons transferred in the electrochemical reaction, *F* is the Faraday constant (96485.3399 C/mol), and *M* is the molecular weight of the active materials.

(f) Specific charge/discharge capacity (Q_c or Q_d)

(Q_c or Q_d) can be calculated by the total amount of charge transferred in the following equation:

$$\text{Qc (or Qd)} = \frac{I \times t}{m} \quad (2.3)$$

Where I represents the current (mA), t is the time (h), and m is the mass of active materials.

So that Q_c or Q_d is in units of mA h g^{-1}.

(g) Specific energy

The specific energy can be described as the amount of energy that can be delivered in a constant mass or volume. The terms specific energy (*SE*) is expressed in units of Wh/kg, and energy density (*ED*) is expressed in units of Wh/L.

$$SE = \frac{E \times Q}{1000} \tag{2.4}$$

$$ED = \frac{E \times Q \times m}{1000 \times V} \tag{2.5}$$

Where *E* is the voltage (V), *Q* is the specific capacity (mAh kg^{-1}), *m* is the weight of the cell (kg), and *V* is the volume of the cell (L).

(h) Power

Specific power (*SP*, expressed in watts per kilogram, W/kg) and power density (*PD*, in watts per liter, W/L) is the ability of the cell to deliver power per unit mass and per unit volume, respectively.

$$SP = \frac{SE}{t} \tag{2.6}$$

$$PD = \frac{ED}{t} \tag{2.7}$$

Where *t* is the discharge time (hours).

(i) Coulombic efficiency

Coulombic efficiency represents the ratio between the energy eliminated from a battery during discharge compared to the energy used during charge. It is expressed as a percentage.

$$\eta = \frac{n^{th}Q_d}{n^{th}Q_c} \times 100\% \tag{2.8}$$

(j) Rate capacity

The term charge/discharge rate or C-rate is usually used to represent the speed of charge and discharge, which can be regarded as the fraction of the rated capacity of the battery that is conveyed in ampere-hours (A.h). For instance, C/5 (0.2 C) means a full charge/discharge (one cycle) would take 5 h. Namely, a larger denominator in the term rate means a longer time to finish one cycle of charge/discharge.

(k) Short Circuiting

A short circuit is an electrical circuit that allows a current to travel along an unintended path, often where essentially no (or a very low) electrical impedance is encountered. A large current can cause rapidly increasing heat, sometimes causing damage to the wire's insulation or a fire.

(l) Irreversible capacity

Irreversible capacity is a parameter to demonstrate the capacity loss after running each cycle.

For anode materials:

$$\text{Irreversible capacity} = n^{th}Q_d - n^{th}Q_c \quad (2.9)$$

For cathode materials:

$$\text{Irreversible capacity} = n^{th}Q_c - n^{th}Q_d \quad (2.10)$$

Irreversible capacity is a significant factor that can reflect the stability of the cells during charge and discharge process.

2. 2 Cathode materials for Sodium-ion batteries

The cathode materials for sodium-ion batteries can currently be divided into three main different types: (1) layered sodium transition metal oxides (Na_xMO_2), (2) sodium metal phosphates ($NaMPO_4$), (3) sodium metal fluorides (Na_xMF_3). Therefore, an introduction is presented on each of the above three types of advanced materials.

2.2.1 Sodium transition metal oxide (Na_xMO_2)

In the 1980s, Delmas.et al. was the first to synthesize four different phases of sodium cobalt oxide, O3, O′3, P3, and P2 respectively.[14] At that time, sodium cobalt oxide was attracting great attention due to its high specific energy, 260Wh/kg and operating potential 2~3.5V (vs. Na^+/Na), and quite good stability. Arienzo et al. used Co_3O_4 as the precursor for hydrothermal synthesis of $Na_{0.71}CoO_2$, with a capacity of 120, 105,and 80mAh g^{-1} at the current density of 5, 20, and 40mA g^{-1}, respectively.[15] Later, Yabuuchi synthesized a new P2-$Na_{2/3}[Fe_{1/2}Mn_{1/2}]O_2$ compound which had better electrochemical performance (190mAh g^{-1} at 13mA g^{-1} in the first cycle).[16] Liu et al. creatively used NaV_6O_{15} as cathode because it has excellent cycling stability and rate capability. When the current density was 20, 50, 100,

and 200mA g^{-1}, the capacity was 142, 106, 92, and 78mAh g^{-1}, respectively. After 30 cycles, it still has the capacity of 61mAh g^{-1}, which is reasonably high for that time.[17] Figure 2.5 presents the structure of one type of $Na_{0.44}MnO_2$. In brief, sodium transition metal oxide has become a promising material owing to the following reasons:

1) Easy to synthesize
2) Environmental friendliness
3) High potential and good cycling retention

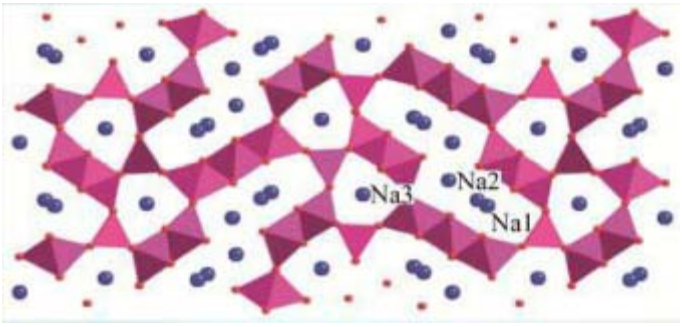

Figure 2.5 the structure of $Na_{0.44}MnO_2$.[18]

It still has certain limitations, however. Firstly, these kinds of materials suffer a dramatic degradation of capacity when the voltage is high (above 4V). Secondly, the sodium ion has a bigger radius than the lithium ion, which makes it harder to insert into or extract from the transition metal oxide.

In order to overcome these drawbacks mentioned above, great efforts have been made. Among all the various approaches, carbon doping was considered to be an effective way to improve the performance of the cathode because carbon could separate the electrode material and the electrolyte, which slows down the formation of the solid electrolyte interphase (SEI) film. Furthermore, the carbon coating layer can increase the conductivity of sodium ions. Ding et al. reported that carbon-coated $NaCrO_2$ ($NaCrO_2$-C) had a higher reversible capacity and better cycling stability than $NaCrO_2$.[19] When the current density

was 5mA g^{-1}, the capacity of $NaCrO_2$-C and $NaCrO_2$ was 116 and 106mA g^{-1}, respectively. After 40 cycles, the capacity dropped to 110 and 90mA g^{-1}, respectively.

2.2.2. Sodium metal phosphates

Sodium metal phosphates can also be divided into three different types:

1)$NaMPO_4$ (M=Fe, Mn…..)
2)$Na_xM_2(PO_4)_3$ (M=V, Ti….)
3)$NaMPO_4F$ (M=Fe, Co, Ni, Mn….)

(1) $NaMPO_4$

$NaMPO_4$ also receives great attentions for the cathode material in sodium-ion batteries because $LiMPO_4$ is a well-known cathode material in lithium-ion batteries. $NaFePO_4$ which have several advantages, good capacity (nearly 150mAh g^{-1}), non-toxicity and environmental friendly, is regarded as one of the promising materials among all the candidates. The typical equation is as follows:

$$xNaFePO4 \rightarrow xNa^{+} + xe^{-} + xFePO_4 + (1-x)NaFePO_4 \quad (2.11)$$

$$xLiFePO4 \rightarrow xFePO4 + xLi^{+} + xe^{-} + (1-x)FePO4 \quad (2.12)$$

$NaFePO_4$ also has its drawbacks, however. There are only a few methods to synthesize this material, and the methods are quite complex. Therefore, to find an easier way to synthesize the $NaFePO_4$ is the most important aspect for improving the electrochemical performance. The structures of $NaFePO_4$ and $LiFePO_4$are shown in Figure 2.6.[20]

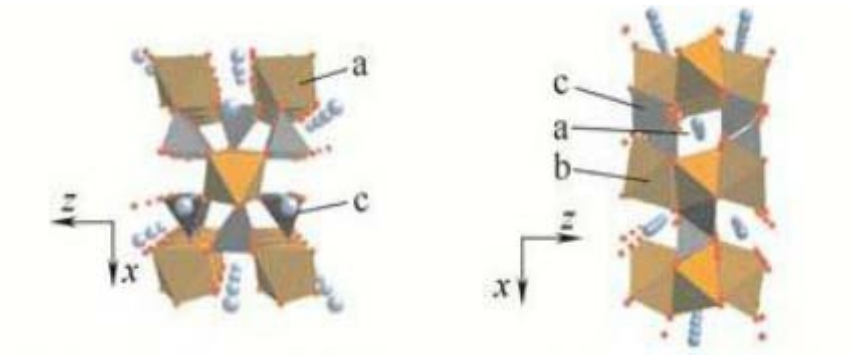

(a)$NaFePO_4$ (b) $LiFePO_4$

Figure 2.6 Comparison of structures of $NaFePO_4$ and $LiFePO_4$.[20]

(2) $Na_xM_2(PO_4)_3$ (M=V, Ti….)

$Na_xM_2(PO_4)_3$ (M=V, Ti….) is a new material for Na^+ ion batteries, which has a special three dimensional path for ion conduction. $Na_3V_2(PO_4)_3$, with good cycling stability, rate performance, and capacity, is regarded as the representative for this kind of material.[21] Du et al.[22] reported that a cell which used $Na_3V_2(PO_4)_3$ as cathode and $LiPF_6$-EC:DEC:DMC=1:1:1, where EC is ethylene carbonate, DEC is diethyl carbonate, and DMC is dimethyl carbonate, as the electrolyte exhibits excellent cycling stability. When the current density is 0.1C, the capacity of the first cycle can reach as high as 114.2mAh g^{-1}, and 97.4% of the capacity is retained after 100 cycles. What is more, it also has excellent rate performance. With the current density of 0.1C, 0.5C, 1C, 2C, 5C, and 10C, the capacity is 114.2, 109.3, 107.0, 104.9, 100.5, and 84.4mAh g^{-1}, respectively. To get better electrochemical performance, Hu et al. [23] creatively presented a new type of carbon-coated $Na_3V_2(PO_4)_3$. This material, $Na_3V_2(PO_4)_3$/C, can provide a voltage of 3.4V, which is much higher than for most cathode materials for sodium-ion batteries. Furthermore, the reversible capacity can reach as high as 100mAh g^{-1}, which is close to the theoretical capacity (117mAh g^{-1}). The coulombic efficiency is calculated to be 98%, which is very high. After 80 cycles, the retention of capacity is 93% versus the first cycle capacity. In brief, this environmentally friendly material, $Na_xM_2(PO_4)_3$, seems to be a promising candidate for the future.

(3) $NaMPO_4F$ (M=Fe, Co, Ni, Mn….)

$NaMPO_4F$ (M=Fe, Co, Ni, Mn,…) with a high voltage (3.7V versus Na+/Na), relatively high capacity (82mAh g^{-1}), and good ion insertion capability has been receiving great attention. Among all these kinds of materials, Na_XFePO_4F can be identified as the commonly used material. Nazar et al.[24] were the first to report that Na_xFePO_4F could be used as the cathode material for a 3.5V (vs Li^+/Li) hybrid sodium lithium battery. They explained that this material can realize the insertion of only one sodium ion. During the charge and discharge processes, the Na_2FePO_4F is transformed to $NaFePO_4F$ and reverses back to Na_2FePO_4F. Langrock et al.[25] reported a carbon-coated Na_2FePO_4F with decent cycling performance. The capacity remains 60mAh g^{-1} after 750 cycles at the current density of 1C, which is mainly attributed to the carbon coating layer. Recham et al.[26] were the first to synthesize super-small Na_2FePO_4F nanoparticles, whose size was only 2.5nm. This kind of nanoparticle can not only dramatically increase the reversible capacity, but also improves the cycling performance. Moreover, it can decrease the effect of voltage polarization. Although $NaMPO_4F$ has excellent electrochemical performance, it also has its shortcomings. The biggest problem is that it will obviously produce a gas including fluoride. At the same time, the manufacturing technique for this material is very complex.[27] Figure 2.7 shows the crystal structure of Na_2FePO_4F.[28]

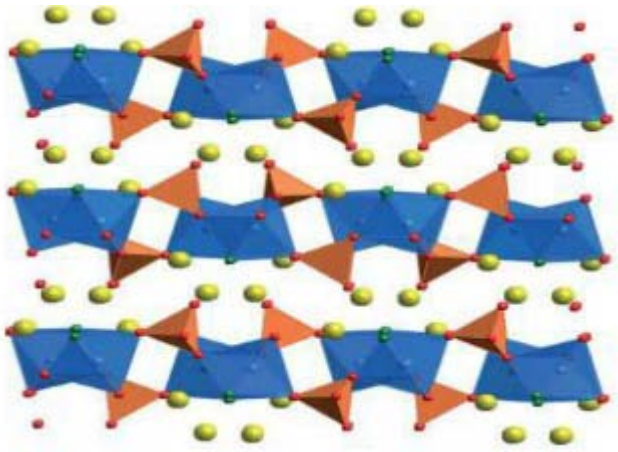

Figure 2.7 Crystal structure of Na_2FePO_4F.[28]

2.2.3 Sodium metal fluoride (Na_xMF_3)

Sodium metal fluoride has been developed rapidly in the past twenty years. Gocheva et al. [29] were the first to synthesize $NaMF_3$ (M=Fe, Mn, Ni) compounds by a simple mechanical method. They proved that the $NaMF_3$ made from MF_2 and NaF could still be active at low temperature. Under the conditions of 1.5V–4.0V and0.2mA cm^{-2}, $NaFeF_3$ still has a reversible capacity of 120mAh g^{-1}, while $NaMnF_3$ and $NaNiF_3$ show poor electrochemical performance and need some improvement. Okada et al. [30, 31] synthesized a series of metal fluorides such as $NaFeF_3$, $NaMnF_3$ and $NaNiF_3$, for systematic research. When the voltage ranges from 1.5V–4.5V with a current density of 0.076mA cm^{-2}, the capacity of the first cycle can reach 197mAh g^{-1}, which is outstanding among all the sodium materials. According to the X-ray photoelectron spectroscopy (XPS) results, it was demonstrated that the Fe^{2+} and Fe^{3+} ions are transformed reversibly by reduction and oxidation. In addition, Okada also did research on using the FeF_3 as the sodium-ion battery cathode. When the upper voltage window was restricted to 2V (vs. Na^+/Na), the reversible capacity was 100mAh g^{-1} following the reduction from Fe^{3+} to Fe^{2+}. When the upper voltage window was kept at 0.85V, the Fe^{2+} was transformed to Fe^0 with a high discharge capacity of 700mAh g^{-1}. The material cannot be used directly as cathode, however, because, although the metal fluoride has the capability for sodium insertion, it still keeps in the state lacking of sodium.

2. 3 Anode materials for sodium-ion battery

2.3.1 Carbon anode materials

Carbon is one of the most basic elements in nature, which has a large variety of complex structures due to the different source, such as oil, pitch, coal tar, benzene, graphite, polymer resins, etc., and different methods of preparation. Figure 2.8 shows various kinds of carbon that are used in batteries.[32]

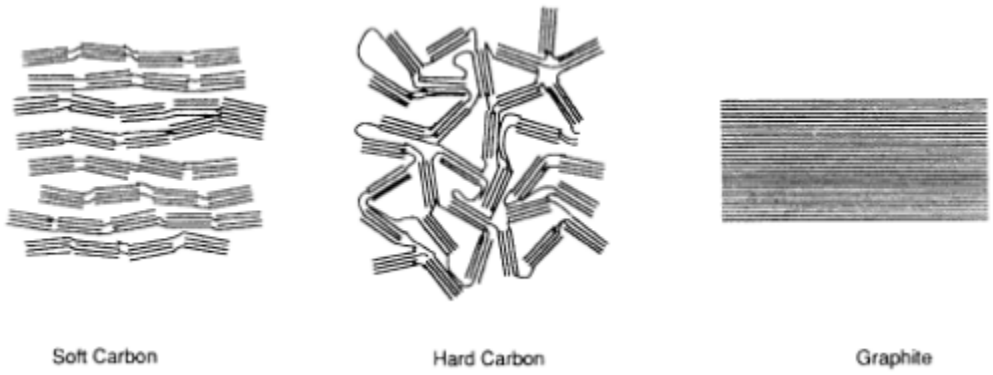

Figure 2.8 Schematic diagram of the structures of three different types of carbon. [32]

As is well known, carbonaceous-based materials are regarded as the most promising materials for producing anodes in rechargeable lithium batteries, since they went into widespread use by Sony Laboratories due to their low cost, environmental friendliness, cycling stability and good capacity retention.[33] Graphite compounds with a theoretical capacity of 372mAh g^{-1} tend to be outstanding among all the anode materials for lithium-ion batteries. Graphite, however, seems not to be used as anode material for sodium-ion batteries because the sodium ion has a larger radius than the lithium ion, which leads to difficulties in the extraction from graphite, as shown in Fig. 2.9. [34-36]

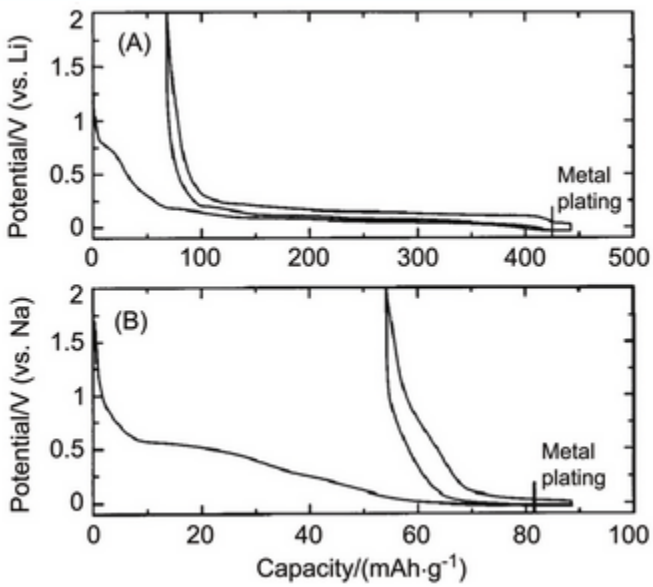

Figure 2.9 Electrochemical profiles of graphite in lithium ion batteries (A) and sodium ion batteries (B).[35]

Up to now, much effort had been made to modify the characteristics of carbon anode materials. Alcantara et al.[37] used amorphous and porous carbon black as the anode for sodium-ion batteries. The electrolyte they used was$NaClO_4$-EC: DMC (1:1). The cathode material was $Na_{0.7}CoO_2$. The reversible capacity is nearly 200mAh g^{-1}, which is acceptable. Komaba et al.[38] reported a cell whose coulombic efficiency could reach up to 90% in the first cycle, and there was still a capacity of 220mAh g^{-1} after 100 cycles. This is mainly because of improvement of the electrolyte and the change in the microstructure of the carbon. Tang et al.[39] mentioned a hollow carbon nanotube which was synthesized by a hydrothermal method. This kind of materials exhibits excellent cycling stability and rate capacity performance. The first discharge capacity is 537mAh g^{-1} with a voltage ranged from 0~3V (vs. Na^+/Na) and a current density of 50mA g^{-1}. Then in the first ten cycles, the capacity drops dramatically.

After 100 cycles, the capacity remains 200mAh g^{-1}. When the current density is 0.2, 0.5, 1.2, 5 and 10 A g^{-1}, the capacity is 168, 142, 120, 100, 75 and 50mAh g^{-1} respectively. The electrochemical performance of this material is excellent mainly because of the reasons mentioned below:

1) The special hollow structure can protect the continuous conductivity of ions.
2) The contact surface between the electrode and electrolyte of this material is bigger than in others, which provides much more locations for transferring ions.
3) The big layered structure makes sodium ions easier to transfer.

Cao et al.[40] reported a hollow carbon nanowire for sodium ion batteries. When the current density was 50, 125, 250, and 500mA g^{-1}, the capacity was 252, 238, 216, and 149mAh g^{-1},

respectively. The electrochemical performance is quite good. Gotoh et al.[41] traced the process by which sodium ions intercalate into the hard carbon. The principle can be described as in Figure 2.10.[42]

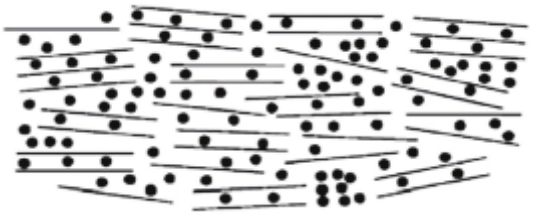

Figure 2.10 Representation of the behaviours of which sodium intercalates into hard carbon.[42]

In conclusion, the main way to improve the electrochemical performance of sodium-ion batteries is to find an anode material which allows easier extraction of sodium ions. Nowadays, the ways to synthesize the carbonaceous material for anode are quite complicated.

2.3.2 Alloy based anode materials

Alloy anodes are regarded as promising anode materials for sodium-ion batteries due to their safety characteristics and high capacity. [43-46] Sodium can alloy with many transition metals, e.g., Si, Sn, Sb, P, Mg, Ge, and Zn. Obviously, not all the elements mentioned above have been researched because of many factors, such as price, safety, and abundance. Alloy-based anode materials include not only pure metals and alloys, but also their intermetallic compounds, either in the crystalline or the amorphous state.

Table 2.2 makes a comparison of the electrochemical properties of alloy anodes for lithium-ion batteries. [47]

Materials	C	Si	Sn	Sb	Al	Mg
Density(g/cm)	2.25	2.33	7.29	6.7	2.7	1.3
Theoretical specific Capacity(mAh g^{-1})	372	4200	994	660	993	3350
Theoretical charge density (mAh cm^{-3})	837	9786	7846	4422	2681	4955
Volume change(%)	12	320	260	200	96	100

Table 2.2 Comparison of the theoretical specific capacity, charge density, density and volume change of various anode materials for sodium ion batteries.[47]

Although many alloy-based materials can reaches high capacity, such as $Na_{15}Sn_4$ (847 mA h g^{-1}), Na_3Sb (660mAh g^{-1}) and Na_3Ge (1108mAh g^{-1}), alloy-based materials still have their drawbacks.[48-54] The alloy anodes have poor cycling stability due to their large volume changes, as shown in the Table 2.2 during the sodium insertion and extraction. What is more, the alloy anodes suffer from high irreversible capacity loss in the first cycle, which makes them hard to use for practical applications. This is mainly because of:

(1) The formation of solid-electrolyte interphase (SEI) films
(2) Loss of active material
(3) Aggregation of alloy particles
(4) Reaction with surface oxide layers

Figure 2.11 presents TEM images of the formation of solid-electrolyte interphase (SEI) films.

(a) (b)

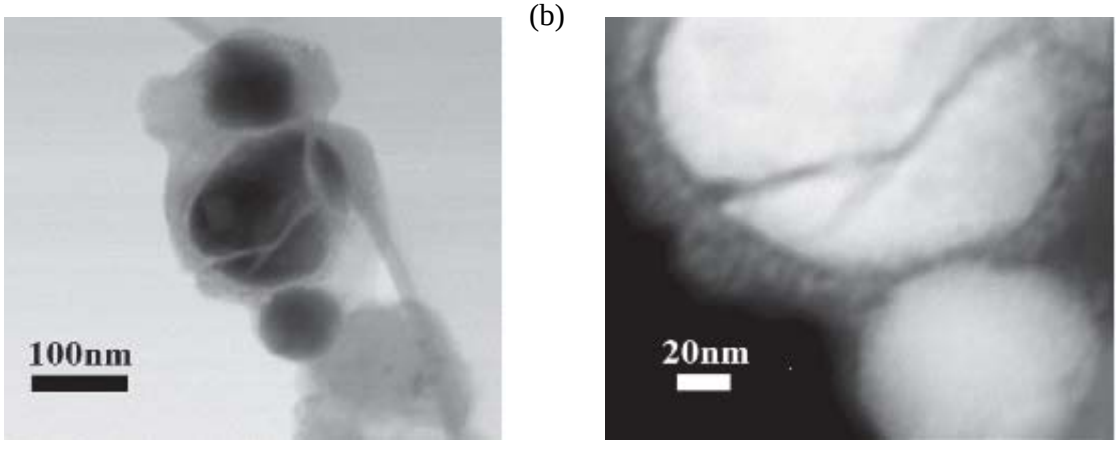

Figure 2.11 Low and high magnification TEM images of the formation of solid-electrolyte interphase (SEI) films after 80cycles at the 0.2C rate.[55]

From Figure 2.11, it can obviously be seen that the appearance of the SEI films accompanies the charge and discharge process. In the formation of SEI films, the electrolyte is first reduced so that it hinders the conductivity of ions. Extensive research has been carried out to find alloy materials suitable for application. Baggett et al.[56] reported a method for synthesizing Cu_2Sb nano-thin films for anodes in sodium-ion batteries. The voltage of this material is 0.5V (vs. Na^+/Na) with a reversible capacity of 250mAh g^{-1}, and its theoretical capacity is 323mAh g^{-1}. Even under the current density of 10C, the cell still can provide a capacity of 226mAh g^{-1} in the initial cycle. Qian et al.[57, 58] used a simple method to synthesize the Sb/C compounds. The Sb/C material has excellent capability for extraction of sodium ions. In the first cycle, the capacity is 610mAh g^{-1} with a current density of 100mA g^{-1}. After 100 cycles, the capacity remains 94 percent of that of the first cycle. In addition, the reversible capacity of the cell still can reach up to 309mAh g^{-1}, even under a current density of 2000mAh g^{-1}. Xiao et al.[59] also reported a SnSb/C nanocompound by using the same method as Qian. The initial capacity was 544mAh g^{-1}, and it displayed reasonably good cycling stability and rate performance. The capacity dropped gradually to 435mAh g^{-1} after 50 cycles. The loss of capacity is mainly due to the volume expansion, which changes the structure of the material.

2.4 Binders for the sodium battery

To prepare a battery cell, the active anode materials are mixed with conductive carbon particles and a binder, which is normally from 5% to 15%. The conventional binder used for alloy anodes is polyvinylidene fluoride (PVDF), a thermoplastic material with poor elastomeric properties. Therefore, an alternative elastomeric binder to PVDF is urgently required to accommodate the large volume changes of alloy particles.[60] It has been proved

that cross-linking polymers and an elastomer binder system can improve the cycling stability of different alloy anodes.[61] This concept was challenged, however, when sodium carboxymethyl cellulose (CMC) binder came out. The CMC binder was more effective in enhancing capacity rention,[62] and it suggests that there are other factors which play an important role in addition to elastic elongation. The CMC binder seems to modify the surface to promote the formation of a stable SEI passive layer. Lestriez et al.[63] reported that the CMC led to a more homogeneous dispersion and better networking of the active material and the conductive carbon, while Winter et al. [64] believed that there is formation of strong chemical bonds between the CMC binder and the active materials (Si), which improves the reversibility for Si/C electrode prepared with CMC binder. The cohesive strength plays an important role in the improvement. In addition, the usage of a polyamide-imide (PAI) binder increased the coulombic efficiency of a Si-based electrode from 29% to 75% in the initial cycle. At the same time, a polyacrylate (PAA) binder has shown better performance than CMC binder.[65] The material using PAA binder exhibited excellent capacity retention and rate capability. All these research works indicated that the selection of a binder system plays a significant role in the performance of active materials. There is a still long way to go to really understand the various binder systems.

2.5 Electrolyte for sodium battery

As with the binder mentioned above, the choice of electrolyte also has a significant effect on the cycling stability and irreversible capacity of sodium batteries. The conventionally used electrolytes for sodium-ion batteries can be mainly divided into two types:

(1) $NaPF_6$ dissolved in carbonates, such as ethylene carbonate (EC), dimethyl carbonate (DMC), and diethyl carbonate (DEC).

(2) $NaClO_4$ dissolved in carbonates, such as ethylene carbonate (EC), dimethyl carbonate (DMC), and diethyl carbonate (DEC).

$NaPF_6$ seems to perform well under most conditions except for low temperature. The low temperature performance is limited below -20°C. The high viscosity and transference of the Na^+ ions in the electrolyte may be the main reason for the poor performance in sodium batteries. The choice of electrolyte system plays an important role in the capacity and cycling stability, but it also is critical for the safety of batteries. It is true that the $NaPF_6$ –organic carbonate solution still has its drawbacks. The relatively narrow stability domain requires the use of a high voltage cathode. The high vapour pressure and the flammability obviously trigger concerns about safety and health, which can lead to serious manipulation hazards.

Recently, much research has been done to improve the safety issues of sodium-ion battery electrolyte, including:

(a) Creation of a redox shuttle which can protect from overcharge

(b) New additives for a stable SEI to enhance the thermal stability

(c) Shut-down separators to properly separate the electrolyte and other parts of the cell to prevent thermal runaway

CHAPTER 3 EXPERIMENT

3.1 Materials and chemicals.

The chemicals and materials used in this study for synthesis, characterization and test of electrochemical performance are listed in Table 3.1 below with the details of suppliers.

Table 3.1 Chemicals and materials used in this thesis.

Material/Chemicals	**Formula**	**Purity(%)**	**Supplier**
Polyvinylidenedifluoride(PVDF)	$(CH_2CF_2)n$	N/A	Sigma Aldrich, Australia
Carbon black	C	Super P	Timcal, Belgium
Sodium hexafluorophosphate	$NaPF_6$	99.99	Sigma Aldrich, Australia
Dimethyl carbonate	$C_3H_6O_3$	99+	Sigma Aldrich, Australia
Glucose	$C_{12}H_{22}O_{11}$	99	Sigma Aldrich, Australia

Hydrochloric acid	HCl	36.5	Sigma Aldrich, Australia
Sulphuric acid	H_2SO_4	98	Sigma Aldrich, Australia
Copper foil	Cu	N/A	China
Diethyl carbonate (DEC)	$C_5H_{10}O_3$	99+	Sigma Aldrich, Australia
Ethylene carbonate (EC)	$C_3H_4O_3$	99	Sigma Aldrich, Australia
Tetraglyme	$C_{10}H_{22}O_5$	N/A	Sigma Aldrich, Australia
Pyrrole	C_4H_5N	98	Sigma Aldrich, Australia
Nickel foam	Ni	N/A	China
Acetic acid	CH_3COOH	99.7+	Sigma Aldrich, Australia

			Sigma Aldrich, Australia
Potassium hydroxide	KOH	98	Sigma Aldrich, Australia
Thiourea	$SC(NH_2)_2$	>95	Sigma Aldrich, Australia
Tin(II) chloride dihydrate	$SnCl_2 2H_2O$	96	Sigma Aldrich, Australia
Nitric acid	HNO_3	69	Sigma Aldrich, Australia
Graphite	C	N/A	Sigma Aldrich, Australia
Aluminium foil	Al	N/A	China
CR2032 type coin cells	N/A	N/A	China
Lithium metal	Li	99.9	Sigma Aldrich, Australia
Sodium metal	Na	99.9	Sigma Aldrich, Australia

			Sigma Aldrich, Australia
Polypropylene separator	$(C_3H_6)n$	Celgard 2500	Sigma Aldrich, Australia
Milli-Q Water	H_2O	5 ppb(TOC)	Millipore, USA
Ethanol	C_2H_5OH	Reagent	Q-store, Australia
Pure methanol	C_2H_5OH	99.95% abosolute	Sigma Aldrich, Australia
1-methyl-2-pyrrolidinone (NMP)	C_5H_9NO	99.5	Sigma Aldrich, Australia
Sodium dodecyl benzene sulphonate	SDBS	N/A	Sigma Aldrich, Australia
Carboxymethyl cellulose	CMC	99.5	Sigma Aldrich, Australia
Sodium perchlorate	$NaClO_4$	99.5	Sigma Aldrich, Australia

			Sigma Aldrich, Australia
Iron(III) chloride	$FeCl_3$	97	Sigma Aldrich, Australia
Propylene carbonate	$C_4H_6O_3$	99.5	Sigma Aldrich, Australia
Aniline	C_6H_7N	99.5	Sigma Aldrich, Australia

3.2 Experimental procedures

The research work for this thesis was mainly focused on synthesizing new electrode materials, and the outline of procedures is shown in Figure 3.1. They can be divided into four parts:

(a) Experimental design (thinking about the possibility and feasibility)
(b) Preparation
(c) Physical and morphological characterization
(d) Electrochemical characterization

Nanostructured active materials for sodium-ion batteries were characterized by a series of physical techniques, such as SEM/TEM and so on. Electrochemical measurements were conducted on coin-type cell.

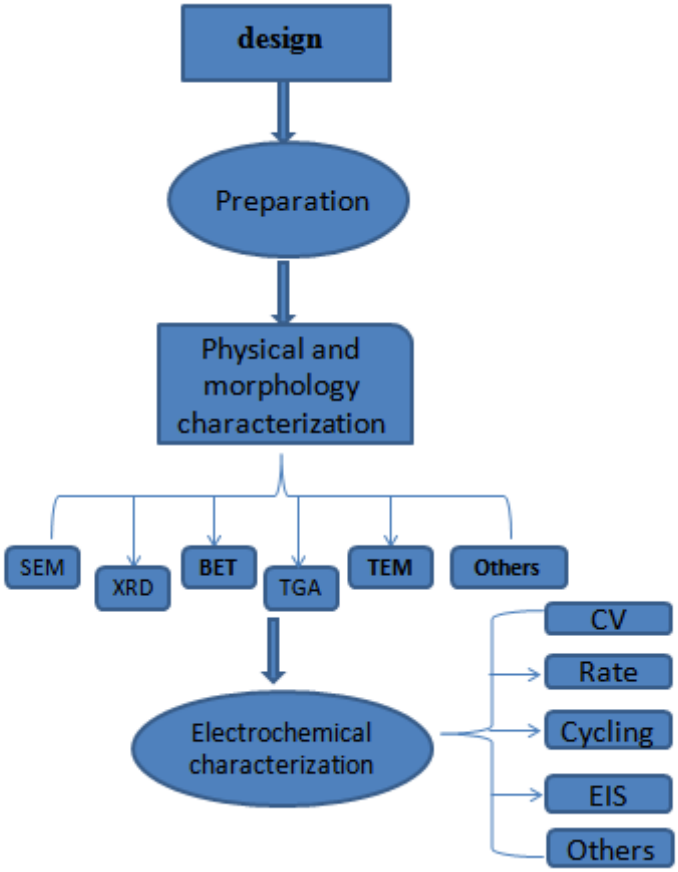

Figure 3.1 Overview of experimental procedures.

3.3 Materials synthesis techniques

The methods which were used in the study are the suction filtration method, the electrospinning method, and the hydrothermal method. The specific details are given as follows:

3.3.1 Suction filtration method

Suction filtration (Figure 3.2) is a widely used technique that can provide superior filtration

capability in the laboratory. Traditional filtration just offers a force which draws the liquid through the filter paper, and suction filtration provides a pressure to push the liquid. In this study, suction filtration was mainly used to obtain material which was diluted in a solution.

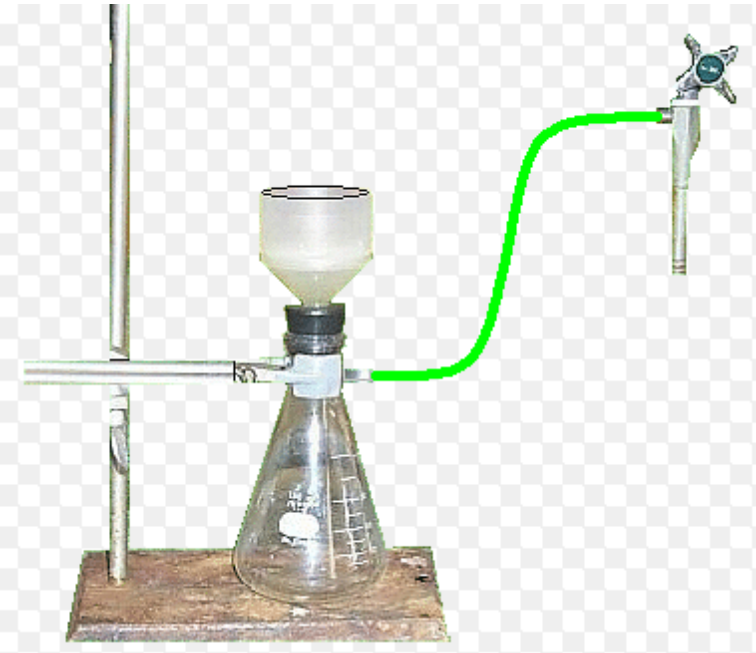

Figure 3.2 Schematic diagram of suction filtration.

3.3.2 Electrospinning deposition method (ESD)

The electrospinning deposition method (Figure 3.3) is a very simple technique which uses a high charge to fabricate uniform fibres or tubes from a solution. It mainly includes three parts: a voltage supply, an injection syringe, and a collector. Because of the voltage difference, the fibres come out from the tip of the syringe and are collected on the collector. It is only necessary to set several parameters, such as the voltage, the flow velocity of the liquid, and the distance between needle and collector.

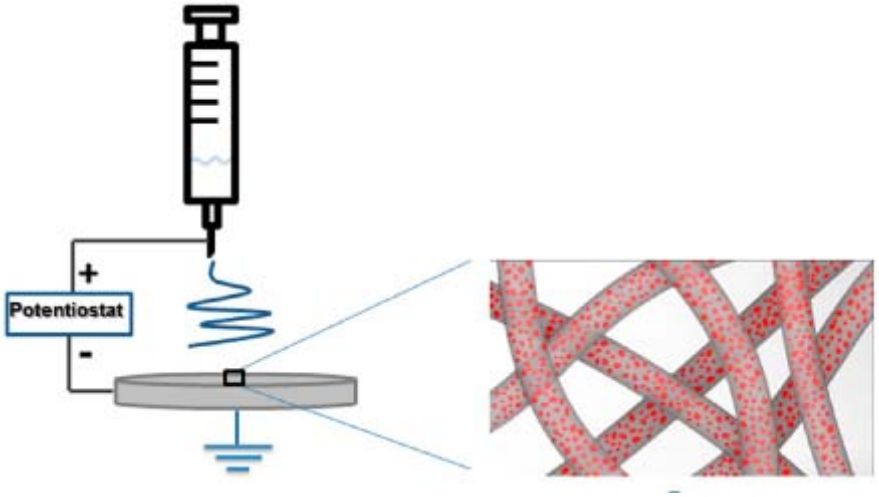

Figure 3.3 Schematic diagram of electrospinning depositon method

3.3.3 Hydrothermal method

The hydrothermal method can produce various morphologies and characteristics of crystallizing substances by using closed-system physical and chemical processes that proceed in aqueous solution at high temperature above 100° C and high vapour pressure above 1 atm.

There are many parameters in this method, such as the duration of the reaction, the temperature, the pressure in the system, and the initial pH of the medium. Among all the parameters, the temperature seems to be the most significant factor, which obviously changes the morphologies and characterization of resulting substances. In my study, the hydrothermal method was used several times, e.g. the synthesis of Graphene-SnO_2 (Gr-SnO_2) and the synthesis of Carbon-coated Graphene-SnO_2 (Gr-SnO_2-C). Normally, the autoclaves, which are shown in Figure 3.4, suffer from a high pressure, so it is important to keep the autoclaves very tightly closed, and the solution volume should be controlled below 2/3 of the volume of the autoclave for preventing boiling, a major safety issue.

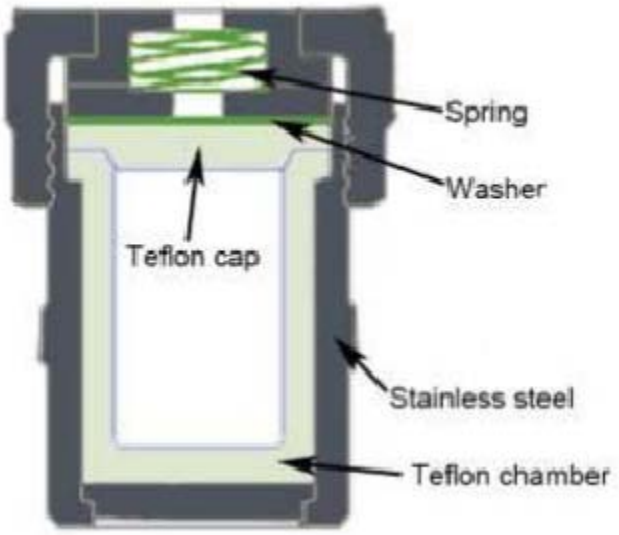

Figure 3.4 Schematic diagram of stainless steel antoclave.

3.4 Characterization and measurement methods

3.4.1 X-ray diffraction (XRD)

X-ray diffraction (XRD) can be used for obtaining the atomic and molecular structures of a crystal, where a beam of X-rays is diffracted by the crystalline atoms in a sample into many specific directions.[66] Usually, unknown substances are identified by powder diffraction, by comparing the final diffraction data against a database of standards, based on the scattering angles and scanning rates, as was the case in my work. For characterization of heterogeneous solid mixtures, this method can also be used to determine the relative abundance of crystalline compounds, and XRD can be coupled with lattice refinement techniques. For instance, Rietveld refinement can provide structural information on particular materials. Meanwhile, XRD also can determine the strains in crystalline materials. A pattern unique to the crystal structure of a given compound results from the scattering from all the different sets of planes. The diffraction condition from planes with spacing, *d*,

can be described by Bragg's law:

$$2d\sin\theta = n\lambda \quad (3.1)$$

where d is the distance between diffracting plans, λ is the wavelength of the incident X-ray beam, n is any integer, and θ is the angle of incidence experienced by the X-ray beam reflection from the faces of the crystal.

The XRD devices used in this thesis were a GBC MMA diffractometer and a BrukerD8-Advanced X-ray diffractometer, both in UOW. Both the XRD devices use Cu Kα radiation, λ = 1.5406 Å.

3.4.2 Scanning electron microscopy (SEM)

A scanning electron microscope (SEM) is a kind of electron microscope which offers images of the morphology of a sample by scanning it with a high energy beam of electrons. The basic mechanism can be summarized as the interaction of high energy electrons with atoms in the sample, which could scatter several different signals that can be detected and provide information on the samples' surface topography and composition. The electron beam is normally scanned in a raster scan pattern, and from each position, the beam builds up the image by the interaction with the sample. The minimum size of the morphology that can be obtained is 1 nm in high vacuum, in low vacuum, and (in environmental SEM) in wet conditions. Energy-dispersive X-ray spectroscopy (EDX) is a particular analytical technique used for the elemental analysis or chemical characterization of a sample, which depends on the interaction of some source of X-ray excitation and a sample. Its characterization capabilities originate to a large extent from the fundamental principle that each element has a unique atomic structure, allowing unique set of peaks on its X-ray spectrum. To stimulate the emission of characteristic X-rays from a specimen, a high-energy beam of electrons, X-rays, or protons is directed onto the sample being studied. The morphology and structures

of samples in this thesis were characterized with a field-emission scanning electron microscope (FESEM, JEOL 7500). Elemental mapping was also conducted on the X-ray spectrometers attached to the JEOL-7500F.

3.4.3 Transmission electron microscopy (TEM)

Transmission electron microscopy (TEM) is another microscopy technique in which a beam of electrons is transmitted through an ultra-thin sample, interacting with the sample as the beam of electrons goes through. From the interaction of the electrons transmitted through the specimen, an image of the sample can be formed, which is magnified and focused on the imaging device, such as a fluorescent screen, a layer of photographic film, or a sensor such as a charge coupled device (CCD) camera.

Because of the small de Broglie wavelength of electrons, TEM can achieve a higher resolution image than light microscopes, which allows the operators to examine fine detail, even as small as a single column of atoms (thousands of times smaller than the smallest resolvable object in a light microscope).

The TEMs used in this thesis were a JEOL 2011, operating at 200 kV, and a JEOL JEM-2010 in UOW and NTU, respectively. Elemental mapping was performed on the X-ray spectrometer attached to the JEM-2100F instrument.

3.4.4 Thermogravimetric Analysis (TGA)

Thermogravimetric analysis or thermal gravimetric analysis (TGA) is a measurement which can detect changes in the physical and chemical properties of materials with increasing temperature at a constant heating rate. In general, TGA is used to determine selected

characteristics of materials that display weight loss or increase because of decomposition, oxidation, or loss of volatiles. In this thesis, TGA was used to determine the carbon or sulphur contents in carbon or sulphur composite materials. TGA was carried out in a Shimadzu DRG-60 or a TA Instruments 2000 in flowing N_2or in air.

3.4.5 Raman spectroscopy

Raman spectroscopy is a spectroscopic technique for the study of the vibrations of chemical bonds and the symmetry of molecules, commonly used in chemistry to identifymaterials.[5] In a Raman spectrometer, a laser light interacts with molecular vibrations, phonons, or other excitations, resulting in the energy of some laser photons being shifted up or down. The shift in energy gives information about the phonon modes in the system. The Raman spectra in this thesis work were collected on a JOBIN Yvon Horiba Raman Spectrometer model HR800, employing a 10 mW helium/neon laser at 632.8 nm.

3.5 Electrode fabrication and cell assembly

3.5.1 Electrode preparation

A working electrode includes the active materials, a conductive agent (carbon black, Super-P), and a binder (carboxymethyl cellulose (CMC), Sigma-Aldrich,) which are mixed with N-methyl-2-pyrrolidinone (NMP) to form a homogeneous slurry, which was spread on Cu foil (for the anode) or Al foil (for the cathode). Then, the prepared electrodes were dried in a vacuum oven at 130° C for 3 hours or at 80° C overnight. Finally, the electrodes were either pressed under a pressure of approximately 3000 kg cm^{-2} for 8s or left without pressing, depending on the materials. After that, the electrode was ready to be assembled into a test

cell.

3.5.2 Cell assembly

The cell assembly was carried out in an Ar-filled glove box. 2032-type coin cells or Swagelok-type cells were used with lithium foil as both the counter and reference electrode and a porous polypropylene film as separator. The specific capacity was calculated based on the mass of active materials in the electrode, and the electrolyte was added when the electrodes were assembled on both sides of the separator. After assembly, the cells were aged 24 hours beforeelectrochemical testing. A schematic diagram of the coin-type cell is shown in Figure 3.5.

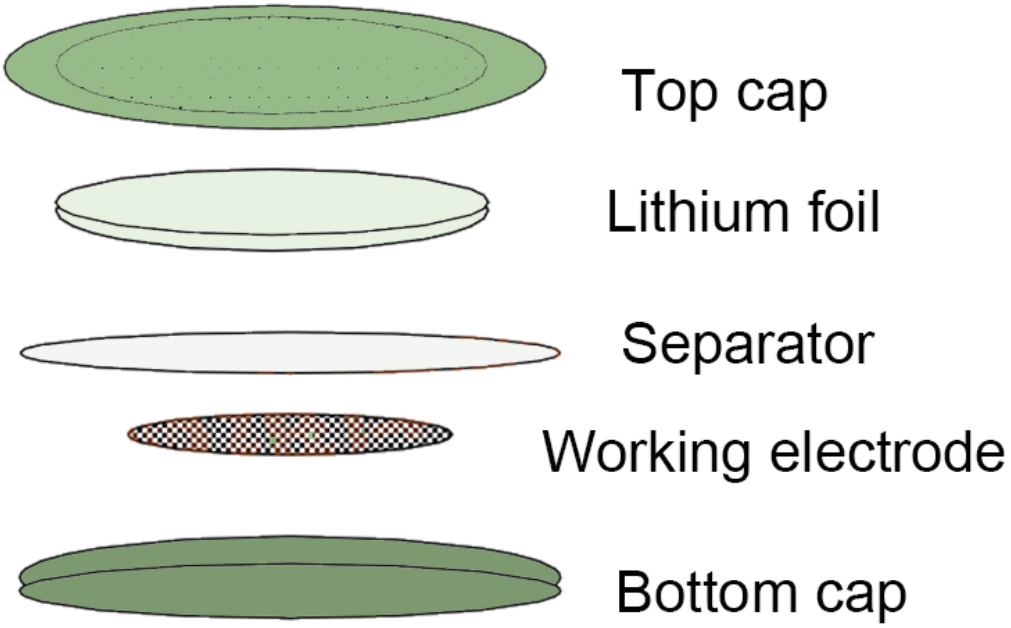

Figure 3.5 Schematic diagram of a coin-type test cell.

3.6 Electrochemical measurements

There are various measurement techniques that are used to evaluate the electrochemical performance in this research work, such as cyclic voltammetry, galvanostatic charging/discharging, and electrochemical impedance microscopy.

3.6.1 Cyclic Voltammetry (CV)

Cyclic Voltammetry (CV) is a unique technique that is used to evaluate the current which develops in an electrochemical cell under conditions where the voltage is in excess of that predicted by the Nernst equation. CV is performed by following the cycling of a working electrode, and testing the resulting current. The potential of the electrode is varied linearly with time, whereas the reference electrode is kept on a constant voltage, and the counter electrode conducts electricity from the signal source to the working electrode. In the study, the CV data were acquired on either an Ametek PARSTAT 2273 electrochemistry workstation or a CHI 660 electrochemical workstation (CH Instrument).

3.6.2 Galvanostatic electrochemical testing

Galvanostatic electrochemical testing is a measurement technique that depends on maintaining a constant current density. The cells can be tested for rate capability at various current densities. In the study, a Land battery tester (China) was used.

3.6.3 Electrochemical Impedance Spectroscopy (EIS)

A common impedance spectrum for active materials consists of a low-frequency semicircle

and a high-frequency linear tail. The semicircle represents the kinetic processes from the charge transfer resistance and the double layer capacitance. The linear tail reflects the solid-state diffusion of Li ions into the bulk of the active materials. In this thesis, EIS data were collected on an Ametek PARSTAT 2273electrochemistry workstation or a CHI 660 electrochemical workstation (CHInstrument).

3. 7 Nomenclature and symbols used in the thesis

3.7.1 Nomenclature

Table 3.2 List of Abbreviations

List of Abbreviations	
Abbreviation	**Full name**
BET	Brunauer-Emmett-Teller
PTFE	Polytetrafluoroethylene
PVDF	Polyvinylidene fluoride
TGA	Thermogravimetric analysis
3D	Three-dimensional
a.u.	Arbitrary unit
SEI	Solid electrolyte interphase
SEM	Scanning electron microscopy

MWCNT	Multi-walled carbon nanotube
SIBs	sodium ion batteries
NMP	1-methyl-2-pyrrolidinone
CCD	Charge-coupled device
CNT	Carbon nanotube
CV	Cyclic voltammetry
TEM	Transmission electron microscopy
SWCNT	Single-walled carbon nanotube
DEC	Diethyl carbonate
EC	Ethylene carbonate
ECs	Electrochemical capacitors
HRTEM	High-resolution transmission electron microscopy
EDX	Energy dispersiveX-ray spectroscopy
EIS	Electrochemical impedance spectroscopy
EV	Electric vehicle
HEV	Hybrid electric vehicle
FE-SEM	Field-emission scanning electron microscopy
XRD	X-ray diffraction

JCPDS	Joint Committee on Powder Diffraction Standards

3.7.2 Symbols

Table 3.3 Symbols

Symbol	Name	unit
2θ	Peak position of XRD	°
C-rate	Charged or discharged rate	mA
Q_c	Specific charge capacity	mAh g^{-1}
Q_d	Specific discharge capacity	mAh g^{-1}
R	Gas constant = 8.319	J K^{-1} mol^{-1}
R_{ct}	Charge transfer resistant	Ω
SBET	Specific BET surface area	m^2 g^{-1}
SE	Specific energy	Wh kg^{-1}
SE	Electrochemically active surface area	m^2 g^{-1}
SP	Specific power	W kg^{-1}
t	Time	h or s
T	Temperature	K or °C
η	Coulombic efficiency	%
λ	X-ray wavelength	Å

L	**Crystal size**	**nm**
m	**Active material weight**	**g**
N	**Avogadro's number = 6.022×10^{-23}**	**mol^{-1}**
P	**Equilibrium pressure**	**P**
P_0	**Saturation pressure**	**P**
PD	**Power density**	**$W\ L^{-1}$**
Q	**Specific capacity**	**$mAh\ kg^{-1}$**

CHAPTER 4 High Capacity and Excellent Cycling Performance of SnSb Carbon Nanofibres for Sodium Ion Battery Anodes

4. 1 Introduction

Lithium (Li)-ion batteries have attracted wide attention for grid-scale energy storage application in the last several years. The price of lithium-ion batteries (LIBs) is dramatically limited, however, by the store of lithium resources. Therefore, sodium-ion batteries (SIBs) are regarded as a substitute for lithium-ion batteries because of both the low cost associated with the high natural abundance of sodium and the decent energy densities, which is similar to those of LIBs.[67-75] Great efforts have been made on sodium ion batteries, but without good performance, simply because the Na ions has the larger radius than the Li ion, which causes the difficulties for rapid ion insertion and extraction, leading to poor cycling stability and low capacity.[76-80] Only a few candidates are capable of reversible insertion/extraction of Na ions.

Nowadays, alloy-based materials are attracting considerable attention because they usually provided high gravimetric and volumetric specific capacity. Similar to Li, Na can also alloy with many metallic elements, such as Si, Sn, P, Sn, Mg, and Zn, and their intermetallics.[81-86] Among all the candidates, transition metals such as tin (Sn), antimony (Sb), and germanium (Ge) are regarded as promising materials because of their high theoretical capacity of 847mAh g^{-1} ($Na_{15}Sn_4$), 660mAh g^{-1} (Na_3Sb), 1108mAh g^{-1} (Na_3Ge) respectively.[86-91] Na alloy reactions also have slightly higher thermodynamic potentials than that of Li, which makes them safer. The large volume change during the sodiation, however, hinders efficient conductivity of ions, leading to low capacity. The alloying reaction between the transition metal and the sodium causes aggregation of metallic particles and electrode pulverization, as well as the regeneration of the solid electrolyte interphase (SEI) film, which leads to rapid deterioration in cycling stability.[92-100] To solve the problems, several strategies have been

put forward to improve the electrochemical performance of sodium ion batteries. Among all the strategies proposed, the use of nanostructure seems to be regards as the most efficient way to improve the properties of energy storage materials. Hence, different kinds of nanostructure have been proposed, such as nanoparticles (NPs), nanowires, nanofibers, nanospheres, nanosheets, etc.[101-105] The nanostructure can not only buffer the massive volume changes and electrode pulverization during charge and discharge, but also improves the ionic conductivity.[106] Recently, Liu et al.[107] reported a single crystalline structure with a capacity of 128 $mAhg^{-1}$after 1000 cycles. Xue et al.[108] proposed a simple nanofiber, which showed excellent cycling stability with 97% capacity retention after 150 cycles.

In this work, we demonstrate a simple approach to make a porous carbon nanofiber (CNF) in which the alloy particles are uniformly distributed for rechargeable SIBs using electrospinning and a thermal treatment process. In this way, the 1-D structure can not only tolerate the massive volume change, but also creates pathways for Na ion conductivity. Having researched various alloy-based elements, we finally chose the SnSb intermetallic phase because of its high theoretical capacity and similarity to pure Sn. As a consequence, the SnSbNP@C composite exhibits a high reversible capacity of 537.9mAh g^{-1} and excellent cycling stability for Na ion storage. After 70 cycles, the capacity remains 98% of the initial capacity, which is about 500mAh g^{-1}.

4. 2 Experimental

4.2.1 Sample preparation

0.65 g polyacrylonitrile (PAN) was first dissolved into 10ml N, N-dimethylformamide (DMF). Then, 3mmol antimony chloride and 3mmol of tin chloride dihydrate were added to the solution at 60°C with vigorous stirring for 24 hours. Finally, the obtained solution was

prepared as the precursor solution for electrospinning. The precursor solution was loaded into a plastic syringe connected to a blunt-tip needle, which was connected to a syringe pump. A voltage of 15kV was supplied between the tip of the needle and the template for electrospinning. The flow rate and distance between the needle and the collector were set to be 0.8ml h^{-1} and 15cm, respectively

.

The products collected after electrospinning were firstly put into an atmosphere-controlled tube furnace and stabilized at 250°C for 10 hours with a heating rate of 2°C min^{-1}. Then, the temperature was increased from 250°C to 600°C under argon(Ar)/hydrogen(H_2) atmosphere with a heating rate of 1°C min^{-1} and maintained at 600°C for 12 hours. A schematic diagram of the procedure is presented in Figure 4.1.

For dispersing agent comparison, 2g polyvinylpyrrolidone (PVP) was also dissolved into 10ml N, N-dimethylformamide (DMF) with the addition of 3mmol antimony chloride and 3mmol tin chloride dehydrate to obtain a solution. The other steps were the same as in the method described above.

For comparison of various materials, 3mmol antimony chloride and 3mmol tin chloride dihydrate were separately added into the PAN-DMF solution to see the difference in electrochemical performance. The other steps were the same as in the method described above.

For electrolyte comparison, different electrolytes such as EC, EC：DMC=1:1 and EC: PC=1:1 with 5%FEC, were used to investigate the difference in electrochemical performance following the same method. PAN-DMF solution was used with the addition of 3mmol antimony chloride and 3mmol tin chloride dihydrate.

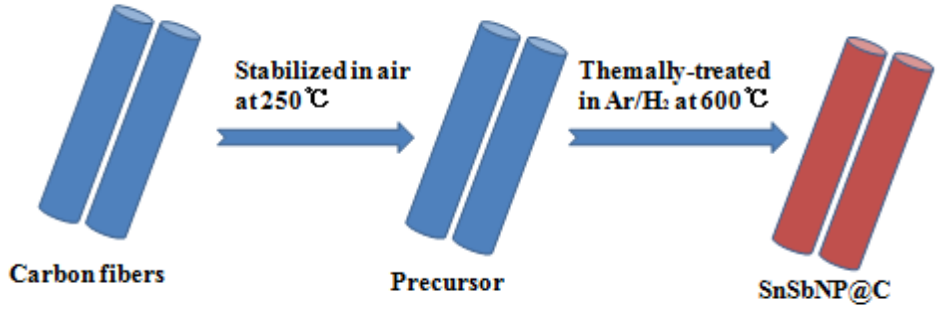

Figure 4.1 Schematic diagram of procedure.

4.2.2 Material characterization

The obtained samples were characterized using powder X-ray diffraction (XRD; GBC MMA diffractometer) with Cu Kα radiation and a scanning rate of $2min^{-1}$. The morphologies of the samples were observed by field emission scanning electron microscopy (FE-SEM; JEOL JSM-7500FA) and transmission electron microscopy (TEM) which was conducted on a JEOL-2010 transmission electron microscope (TEM), operating at 200 Kv with an energy dispersive X-ray spectrometer (EDS). X-ray photoelectron spectroscopy (XPS) was conducted on a VG Multilab 2000. The thermal properties of the samples were characterized by thermogravimetric analysis (TGA; TA Instruments 2000) and heated from 40 to 900°C with a ramp rate of 10°C min^{-1}.

4.2.3 Electrochemical measurements

The electrodes were prepared by mixing 80wt% as-prepared active materials with 10 wt% carboxymethyl cellulose (CMC) binder dissolved in de-ionized water to form a homogeneous slurry. 10 wt% Super P was also added. The electrode slurry was uniformly pasted onto copper foil and dried at 90°C. Electrochemical cells (CR2032) containing the

active materials as working electrode, Na foil as the counter electrode, a glass microfiber film as the separator, and 1M $NaClO_4$ which was dissolved in a 1:1 (v/v) mixture of ethylene carbonate (EC) and, diethyl carbonate (DEC) with 5 wt% fluoroethylene carbonate (FEC) as the electrolyte were assembled in a glove box (H_2O, O_2<0.1 ppm, Mbraun, Ubilab, USA). Electrochemical impedance spectroscopy (EIS) and cyclic voltammetry (CV) were conducted on a VMP-3 electrochemical workstation at a scan rate of 0.1 mV s^{-1}. Galvanostatic charge/discharge was conducted over a voltage range of 0.001-2V versus Na/Na^+ at different constant current densities, which were based on the weight of the samples, tested by a LAND (CT2001A) battery tester.

4. 3 Results and discussion

4.3.1 Stricture and morphologies

To characterize the final substances, X-ray diffraction (XRD) patterns and Raman spectra were collected, as shown in Fig 4.2. All the diffraction peaks in the XRD patterns of the SnSbNP@C-PAN and SnSbNP@C-PVP are almost the same, which index well with the SnSb alloy (JCPDS no. 00-033-0118).[109-114] A small amount of impurity with peaks at 30.7°, 32.0°, 44.2° and 44.9° was attributed to metallic Sn (JCPDS no.00-001-0926).The XRD patterns suggest that the final products can be divided into two parts, mainly SnSb alloy and small amount of metallic Sn. Therefore the following formula is proposed.

$$Sn^{2+} + Sb^{3+} + C \rightarrow Sn_{(1-x)}Sb + xSn + CO_2 \uparrow \qquad (4.1)$$

From the formula, the carbon plays a role in reducing Sn^{2+} and Sb^{3+} into SnSb alloy and Sn. The carbon dioxide released during the carbonization leads to the formation of pores around the SnSb alloy particles, and it also triggers a decrease of content of carbon, which leads to the reduced diameter of the carbon nanofibers. The SnSbNP@C was also characterized by

Raman spectroscopy [Figure 2(b)]. The carbon could be characterized by the graphitic-G band at around~1350cm^{-1} and the disorder-induced D band at around~1580cm^{-1}. According to the results, these two band peak at 1327.27 and 1575.76 cm^{-1}, respectively, corresponding to the Raman curve of Carbon.[115-117] The intensity ratio of the D band to G-band (I_D/I_G) of the composite after carbonization is higher than that for the graphite oxide, indicating the decrease in the average size of the *sp2* domain after reduction.[118, 119]

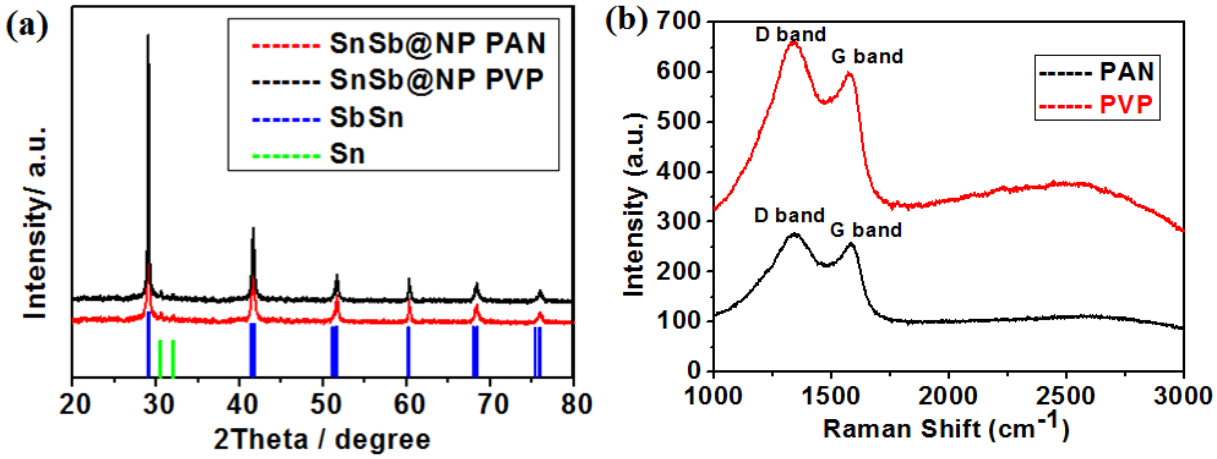

Figure 4.2 XRD patterns (a) and Raman spectra (b) of SnSbNP@C-PAN and SnSbNP@C-PVP composites.

SnSbNP@C-PAN,

Typical scanning electron microscope (SEM) images under (a) low and (b) high magnification of fibers before stabilization at 250° C are shown in Figure 4.3. It can be seen that carbon fibers have the features of smooth surface, uniform diameter of about 300nm and straight line structure. After heat treatment, the diameter of SnSbNP@C decreases to nearly 100nm and the surface becomes relatively tough [Figure4. 3(c, d, e)]. The fibers are also uniformly distributed and show excellent flexibility. What is more, some parts of the fibers gather together to form a flat surface which appears to have the free-standing property, as shown in Figure 4.3(f).

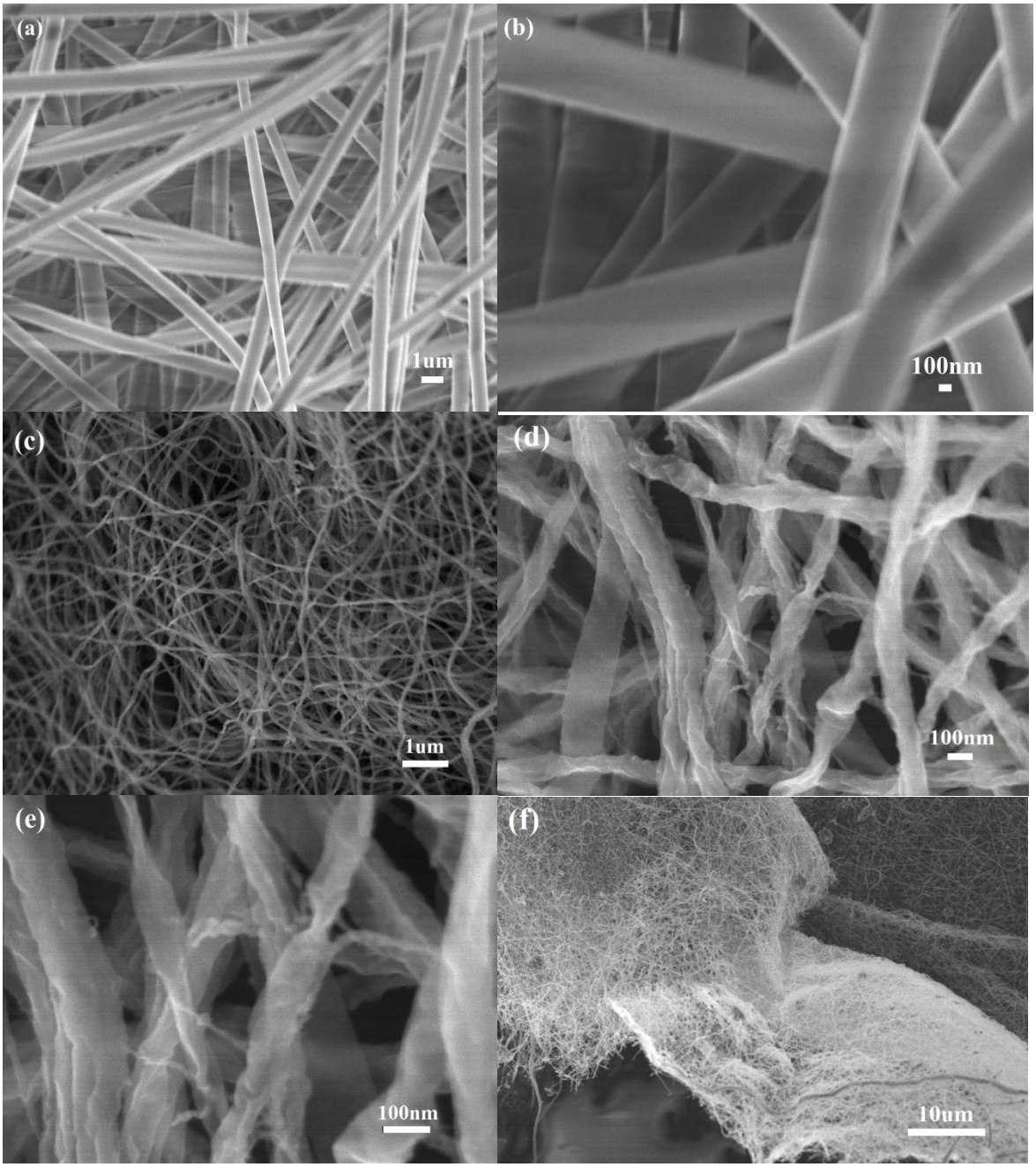

Figure 4.3 SEM images of as-electrospun fibers (a, b) and SnSbNP@C-PAN(c, d, e, and f)

SnSbNP@C-PVP,

Scanning electron microscopy (SEM) technique was also used. The results are shown in

Figure 4.4. The fibers are also distributed uniformly and the diameter of the fibers is around 100nm which seems to be smaller than SnSbNP@C-PAN before stabilization at 250°C, as shown in Figure 4.4(a) and (b). After heat treatment, the surface also becomes rough and the diameter almost remains the same size [Figure 4.4(c) and (d)]. This is probably because the content of carbon in PVP is less than in PAN. There are still a bit charging in this component, which may be caused by the bad conductivity of ions in the surface.

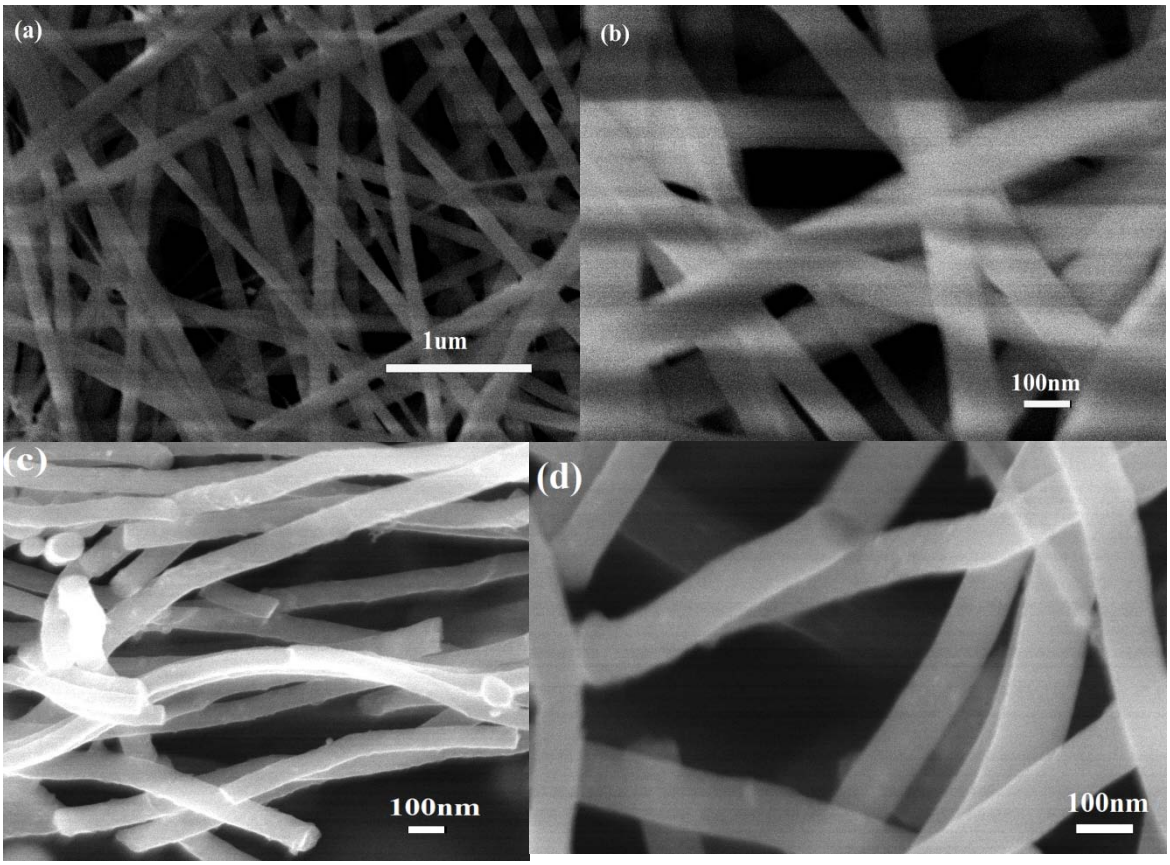

Figure 4.4 SEM images of **S**nSbNP@C-PVP before heat treatment (a, b) and after heat treatment (c, d).

In order to further confirm the presence of SnSb alloy, energy dispersive X-ray (EDX) mapping was conducted. The results are shown in Figure 4.5. The colored points indicate the presence of the respective element. The elements N and C are present due to the PVP/PAN and DMF. From the Figure 4.5, it can be seen that the Sn and Sb are homogeneusly

distributed on both SnSbNP@C-PAN and SnSbNP@C-PVP.

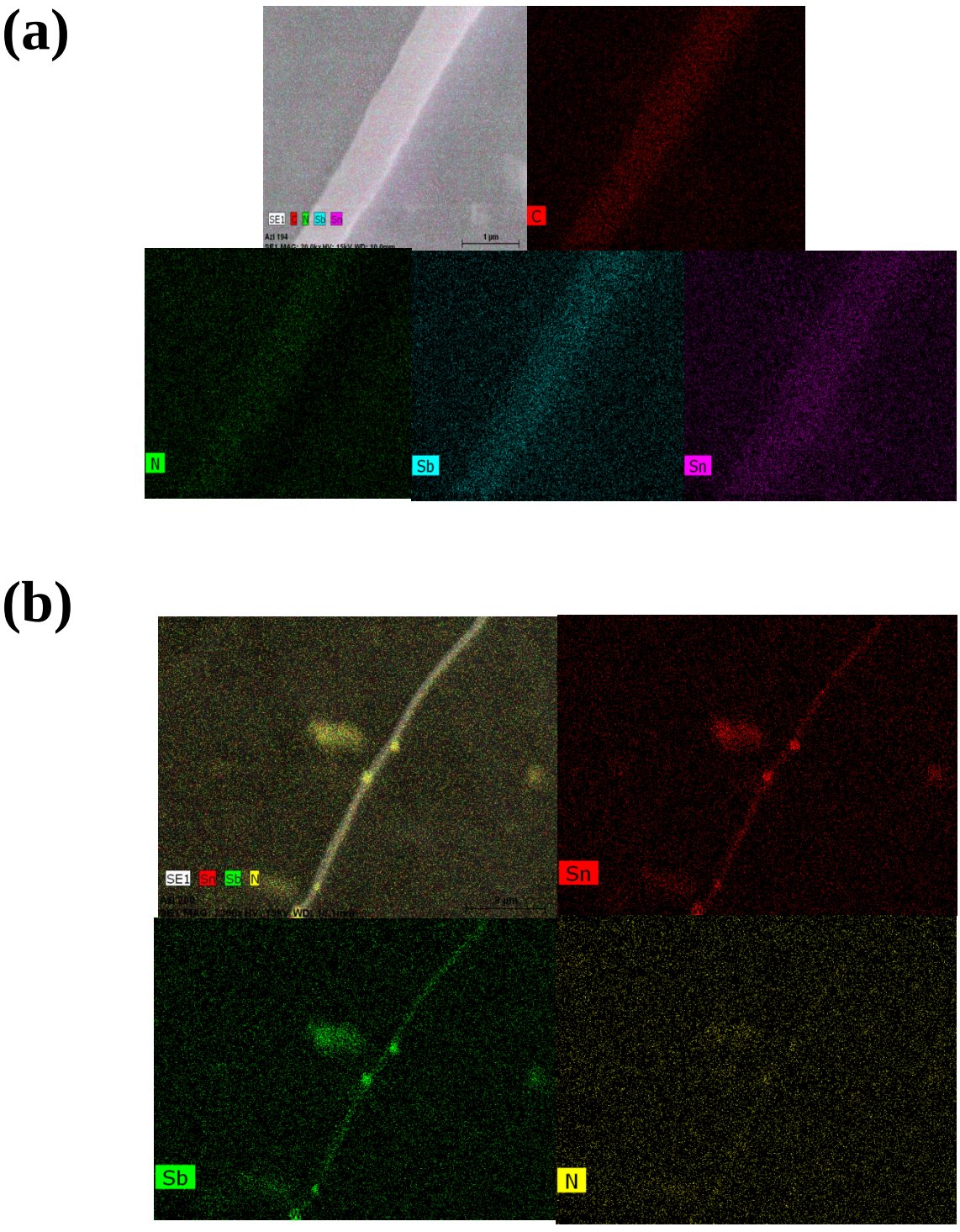

Figure 4.5 EDX mapping of SnSbNP@C-PAN (a) and SnSbNP@C-PVP (b)

SnSbNP@C-PAN,

The transmission electron microscope (TEM) images shown in Figure 4.6 (a, b) clearly display the distribution of SnSb alloy particles. Most of the particles, with an average size of 15nm are distributed within the carbon fibers and only a few particles have grown on the surface of the fibers. To better confirm the composition of the particles, Point a [Figure 3(c)] and Point b [Figure 3(d)] were selected for the EDX mapping. The results demonstrate that Point a is composed of SnSb alloy with a ratio of Sn:Sb=75:25, as is Point b with a ratio of 92:8, respectively, which indicate that there are pure tin metal particles separated out on the surface. The particles distributed on the surface are more likely to be tin metal because the tin was easier to separate out during heat treatment than the antimony, which is consistent with the XRD results mentioned about.

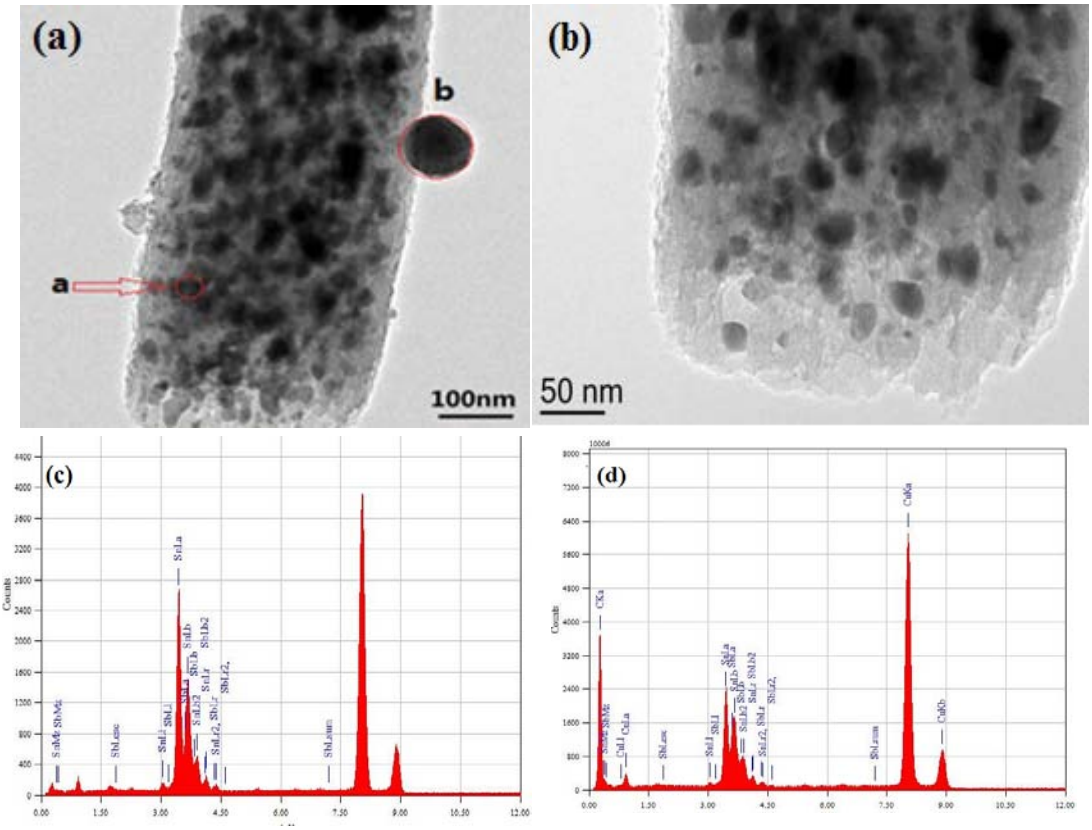

Figure 4.6 Low (a) and high (b) magnification TEM images, with corresponding EDX spectra of Point a (c) and Point b (d).

SnSbNP@C-PVP,

TEM and element mapping were also investigated, as is shown in Figure 4.7. According to the high resolution TEM image [Figure 4.7(b)], there are two sizes of particles that are present in the fibers, while there are no particles on the surface. The average diameter of the big particles is about 20nm, while the average size of the small particles is only 5nm. To better understand the difference between these two size particles. Point C and Point D were randomly selected to do the element mapping. The results demonstrate that both Points C and D are composed of SnSb alloy in the ratio of Sn:Sb=55:45

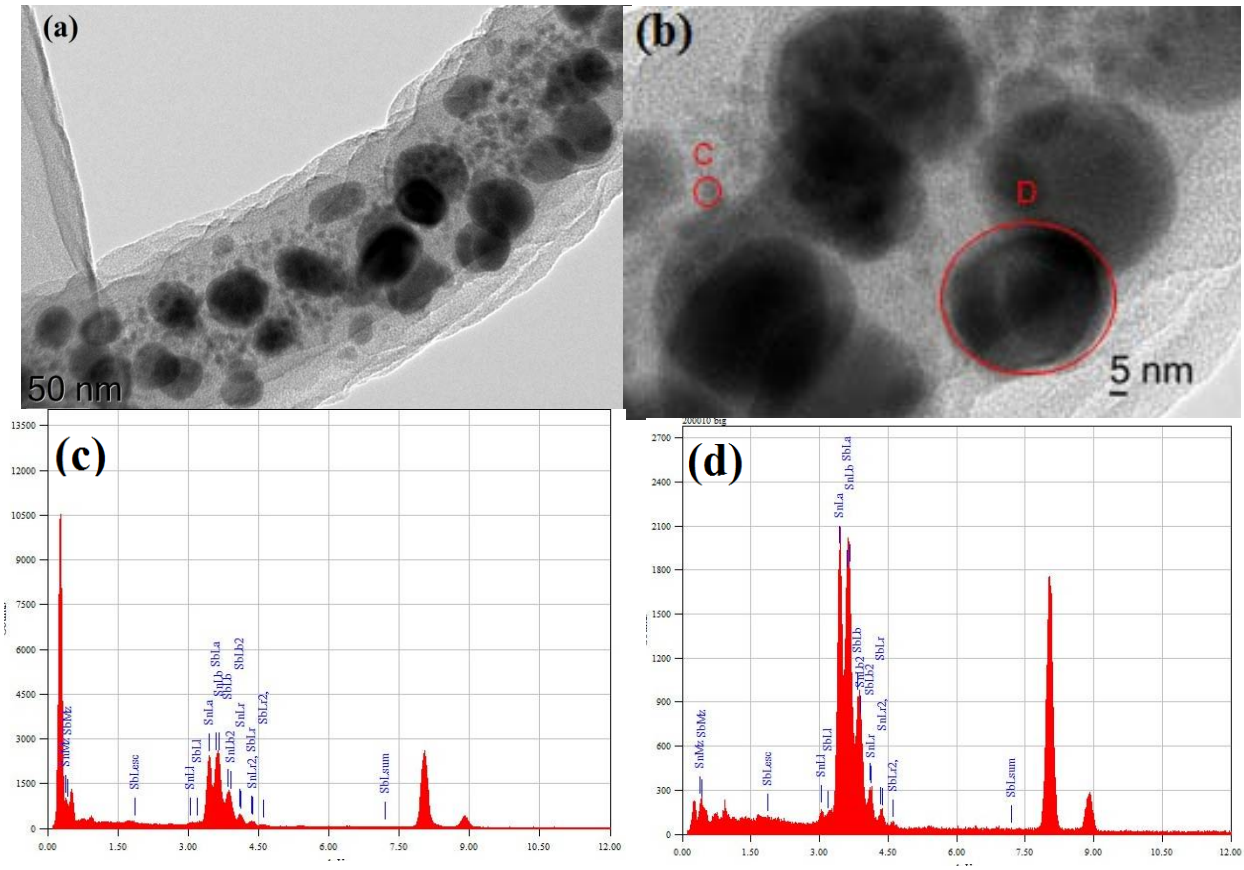

Figure 4.7 Low (a) and high (b) magnification TEM images, and corresponding EDX spectra of Pont C (c) and Point D (d).

The results of thermogravimetric analysis (TGA) are shown in Figure 4.8(a, b). According to the Figure 4.8, it can be concluded that the content of carbon in PAN is larger than that in PVP. In these curves, there are mainly two stages: (1) The Sn and Sb metal is transformed to oxide, in a process which runs from 70°C to 900°C. (2) The carbon burns, transforming to carbon dioxide. The progress of the carbon burning can be divided into two parts also, as the carbon first changes to carbon monoxide at about 350°C and then the carbon monoxide changes to carbon dioxide. 350°C can be regarded as the starting point, which is also in agreement with the results.

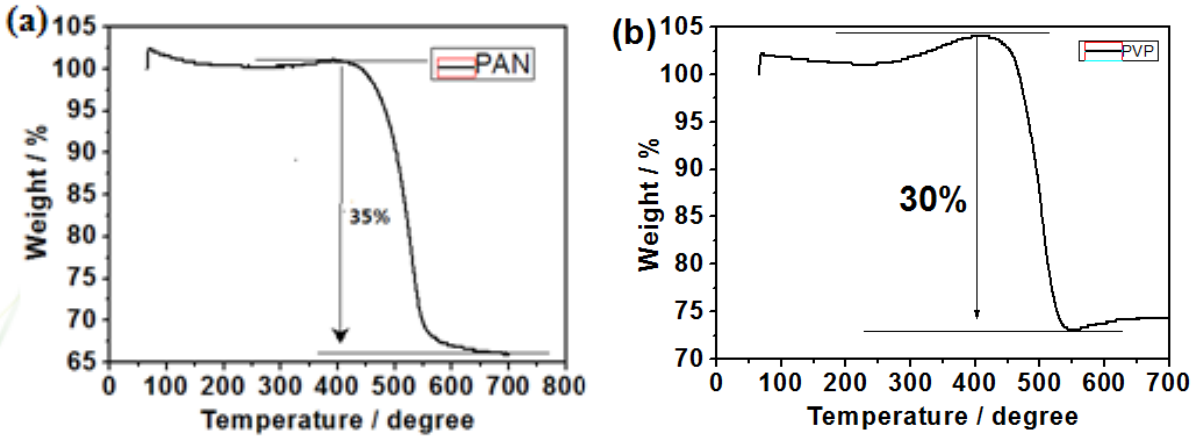

Figure 4.8 TGA curves of SnSbNP@C-PAN (a) and SnSbNP@C-PVP (b).

4.3.2 Electrochemical characterization

Figure 4.9(a) presents cyclic voltammograms (CVs) of the electrodes. It can be observed that there is a reduction peak at around 0.85V, which is mainly due to the irreversible reduction of electrolyte to form the SEI films, and there is another large peak that appears at about 0.25V due to the Na-Sn and Na-Sb alloying reactions to form $Na_{15}Sn_4$ and Na_3Sb alloy compounds during the initial cycle. Furthermore, the areas and positions of the peaks remain the same for the following continuous scan after the activation process, indicating

stable reduction/oxidation reactions.

Figure 4.9(b) shows the voltage profiles of SnSbNP@C-PAN electrode for the 1st, 2nd, and 20th cycles between 0and 2V at the constant current density of 50mAg^{-1}. There is a slope between 1.5V and 0.6V because the first discharge process corresponds to the reduction of SnSb alloy granulesto surface oxide compound. The initial discharge/charge capacities are 768.4mAh g^{-1} and 530.2mAh g^{-1}, respectively, corresponding to an initial coulombic efficiency of 69.0%. After 20 cycles, the electrode still has the discharge capacity of 522.2mAh g^{-1}, indicating its excellent electrochemical reversibility. The irreversible capacity (238.2mAh g^{-1}) is mainly related to the decomposition of electrolyte. The cycling performance is shown in Fig. 4.9(c).The SnSbNP@C-PAN compound has the highest capacity. As is well known, super P provides a stable reversible capacity of 172mAh g^{-1}. With 20 wt% super P in the composite, it may contribute 31.4mAh g^{-1} in capacity. Thus, there is 498.8mAh g^{-1} capacity contributed by the alloy. For a 50%:50% SnSb alloy, the theoretical capacity can be calculated, nearly 753mAh g^{-1} according to Na_3Sb (660mAh g^{-1}) and $Na_{15}Sn_4$ (847mAh g^{-1}), and an 80 wt% SnSb alloy can be assigned a theoretical capacity of 602.4mAh g^{-1}. Therefore, the reversible capacity from the alloy is up to 82.8% of the theoretical capacity, which is quite high. In addition, the reversible capacity remains at about 450mAh g^{-1} after 90 cycles. The capacity retention was 84.9%, which indicates excellent cycling stability. The SnSbNP@C-PVP compound provides an initial capacity of 460.2mAh g^{-1}. After 90 cycles, the capacity drops to 366.9mAh g^{-1}. The fact that SnSbNP@C-PAN compound provides a higher capacity and better cycling performance may be attributed to the following reasons: there is a more uniform distribution of the SnSb alloy particles in the nano-carbon fibers; and the flexible structure may buffer the volume expansion generated during cycling.

As the SnSbNP@C-PAN compound exhibits the best electrochemical performance, it was selected to do rate cycling tests. The rate capability, which is another important parameter

for batteries, was also tested [Fig 4.9(d)].A series of different current densities(30mA g^{-1}, 90mA g^{-1}, 270mA g^{-1}, 810mA g^{-1}, 2430mA g^{-1}, and 7290mA g^{-1}) were used. There is almost no capacity loss for SnSbNP@C-PAN composite electrode using caboxymethyl cellulose (CMC) as a binder after changing the current density from 30mA g^{-1} to 7290mA g^{-1}, and back to 30mA g^{-1} in 70 cycles, which demonstrates the excellent cycling stability and rate performance. In addition, the compound still has a capacity of nearly 230mAh g^{-1} at the high current density of 2430mA g^{-1}, also indicating excellent rate performance.

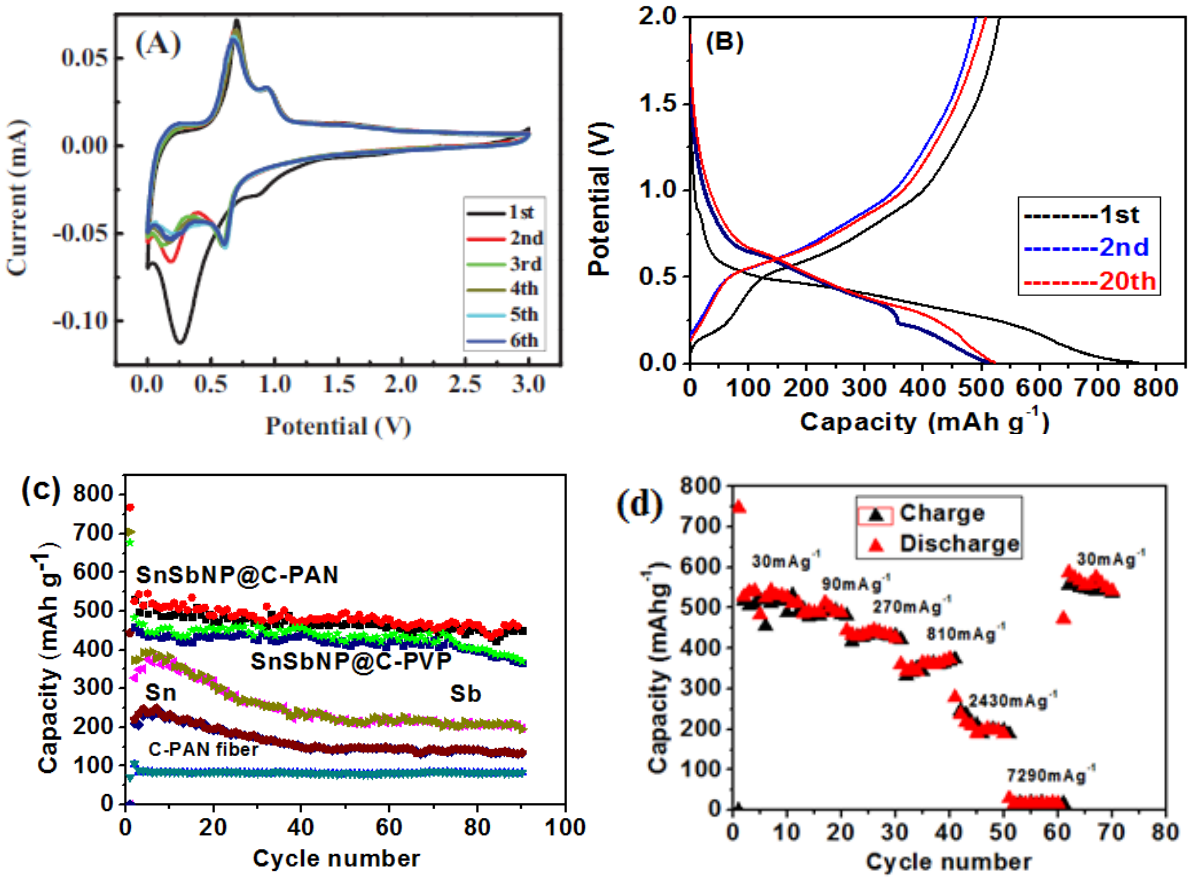

Figure 4.9 (a) CV curves of SnSbNP@C-PAN for the first 6 cycles;(b) galvanostatic charge/discharge voltage profiles for the 1st, 2nd, and 20th cycles of SnSbNP@C-PAN electrode at a current density of 55mAg^{-1};(c) cycling performance of the various electrodes at a current density of 55mAg^{-1};(d) rate capability of the SnSbNP@C-PAN electrode at various current rates from 30mAg^{-1} to 7290mAg^{-1}.

To obtain better electrochemical performance, three main types of electrolytes were selected. The active material was the SnSbNP@C-PAN composite with the CMC binder. The cycling performances in the three types of electrolytes are shown in Figure 4.10. The results illustrate that the electrode which uses electrolyte with FEC has the larger capacity than the one without FEC. This is mainly due to the FEC, which has been confirmed to have an effect on preventing the formation of SEI films.[120-126] In addition, 5%FEC seems to be more suitable than 10%FEC, according to the results in Figure 4.10.

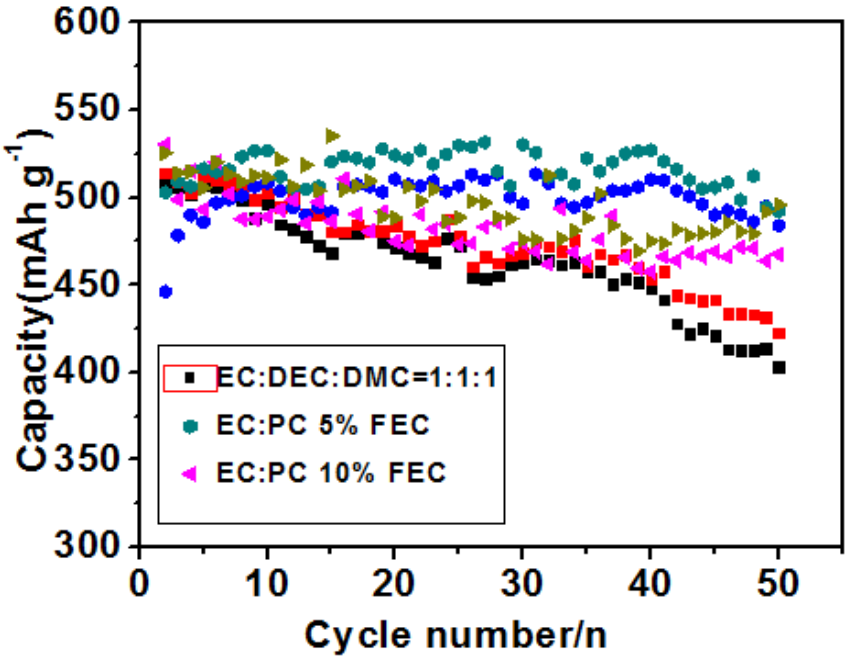

Figure 4.10 Cycling performance of SnSbNP/C-PAN in three different types of electrolytes.

4.4 Conclusions

By using a very simple electrospinning technique and thermal treatment, SnSb nanoparticles are firstly embedded into carbon fiber, and then the pores appear due to the evolution of carbon dioxide gas during thermal treatment. The porous carbon nanofibers, being 1-Dnanostructures, can tolerate the massive volume change during the charge/discharge, and they also create pathways for the conduction of sodium ions which solves the problem that sodium ions are harder to conduct than Li ions because of the large size of their radius. The electrochemical results show that SnSbNP@C-PAN composite provides a capacity of 530mAh g^{-1} in the initial cycle, which is better than those of the SnSbNP@C-PVP composite, pure Sb@C, and pure Sn@C. The rate performance of SnSbNP@C-PAN compound is also excellent, even under the condition of high current density (2430mA g^{-1}). Furthermore, $NaClO_4$ in EC: PC (1:1) with 5%FEC turns out to be the best selection of electrolyte for this material. The FEC plays a significant role in preventing the formation of SEI films, which may trigger the consumption of electrolyte. In conclusion, the SnSb alloy seems to be a promising material that shows high capacity and excellent rate performance as an anode material in sodium-ion batteries.

CHAPTER 5 Synthesis of Tin Sulfide yolk-shell structure with Good Electrochemical Performance in Sodium-ion Batteries

5.1 Introduction

Wide-scale implementation of renewable energy has evoked urgent requirements for the growth of inexpensive and efficient energy storage.[127] Lithium-ion batteries with the merits of high energy density, long cycle life, environmental friendliness, and no memory effect have been widely used in portable electronic devices.[128] There are also many problems occurred in lithium-ion batteries, however, such as relatively short lifetime, poor low-temperature performance, and high cost.[129-135] Furthermore, the increasing demand for Li commodity chemicals will dramatically drive up prices.[136, 137]The sodium-ion batteries (SIBs) were proposed as a substitute for lithium-ion batteries (LIBs) for grid-scale energy storage due to the high natural abundance of sodium and the similarity between sodium and lithium. Among the various active materials, tin (Sn) is a promising material with a high theoretical capacity of 847mAh g^{-1} ($Na_{15}Sn_4$). The main barrier for the use of Sn as an anode material, however, is the volume expansion during sodiation. The alloying reaction between Sn and $Na_{15}Sn_4$ may cause aggregation of Sn particles and electrode pulverization due to the regeneration of the solid electrolyte interphase (SEI) film.

Recently, metal sulphides have been recognised as promising materials because of their high theoretical capacity. A series of metal sulphides, such as NiS, MoS_3, CoS, WS_2, and SnS, has been investigated for Na-ion battery anode materials.[138, 139] Among all the metal sulphides mentioned above, SnS has a unique layered CdI_2-type structure, which is a sandwich-like structure with the tin atoms between two layers of hexagonal close-packed sulphur atoms.[140] This crystallographic feature is suitable for the intercalation of Na ions and can compensate for volume change.

Graphene (Gr), a two-dimensional aromatic monolayer of carbon atoms, has received enormous interest as a promising anode material in energy storage applications due to its excellent electrical conductivity, high specific surface area, and structural flexibility.[141-145] In addition, graphene can be used to host nanostructured electrode materials for energy applications.[146-148] For example, Lee et al. reported the fabrication of graphene with SnS, which gives a reversible capacity of nearly 650mAh g^{-1} in sodium-ion batteries. Guo et al. reported a further fabrication of carbon-coated graphene with SnO_2, which shows excellent rate performance and cycling stability. The graphene sheets and the amorphous carbon coating layer keep the SnO_2 particles wrapped up in the gaps.

Herein, we firstly followed the hydrothermal method of Zhang [149] to obtain the carbon-coated graphene SnO_2 (Gr-SnO_2-C). After we obtained the compound, we creatively used a simple one-pot method to accomplish the sulfidation to get Gr-SnS-C. What is more, the yolk-shell-structure can be obtained by this method. As it is well known, the yolk –shell structure has drawn great attention with its unique distinctive cores, voids, and shells due to its potential application in various fields such as catalysis, nanoreactors, gene delivery as well as its intriguing properties. [150-163] As a result, the Gr-SnS-C might be expected to exhibit synergistic properties and display excellent electrochemical performance with large reversible capacity and good cycling performance for sodium-ion batteries.

5.2 Experimental

5.2.1 Sample preparation

Firstly, the graphite oxide was synthesized by a modified Hummers' method. [14, 15, 22] Graphene oxide (GO) layers were exfoliated from the graphite oxide by using ultrasonication. Tin oxide was grown onto the graphene oxide sheets by a previously

reported hydrothermal method. In this study, 100mg graphite oxide was dispersed into dispersed into 50ml ethanol with ultrasonication for 1.5h to obtain a solution which was marked as solution A. 0.25g tin chloride dihydrate was dissolved in 20ml ethanol to yield the solution B. After mixing solutions A and B, the resultant solution was then transferred to an autoclave, which was kept in an oven at 160° C for 10h. The resultant product was separated and washed several times by centrifugation with de-ionized water after the autoclave was cooled down. Then, the products were dispersed in 20ml de-ionized water following an ultrasonication of 15min. After the ultrasonication, 0.3g glucose was added into the solution following a severe stirring for 20min. Then, it was transferred to an autoclave and kept in an oven at 160° C for 10h. The product was obtained by centrifugation with several washings in de-ionized water after the autoclave was cooled down. The resultant composite was dried at 70° C under vacuum conditions for 24h, followed by heating in a tube furnace under Ar atmosphere at 500° C for 5h, yielding carbon-coated graphene tin oxide (Gr-SnO_2-C).

Next, the obtained Gr-SnO_2-C was transferred into a larger alumina boat with a glass cover. An excessive amount of thiourea powders was loaded into the vacant space in the boat. The loaded boat was put into a tube furnace for heating. When the temperature increased to 350° C, the thiourea powder was melted, which produced hydrogen sulfide gas. The flow rate of air, which was used as the carrier gas, was 5 L min^{-1}. The final product was Gr-SnS-C.

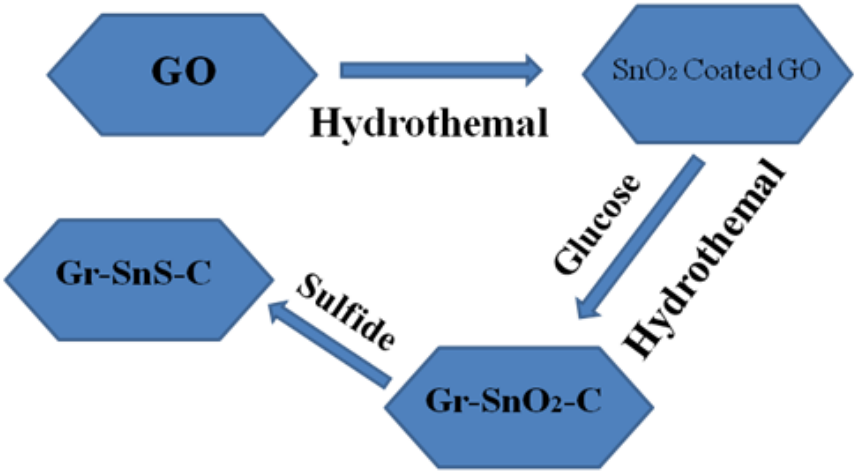

Figure 5.1 Schematic diagram of the experimental procedure.

5.2.2 Materials Characterization

The crystal structure of the as-prepared sample and the powders were investigated by X-ray diffraction (XRD; GBC MMA diffractometer) with Cu Kα radiation at a scanning rate of $2min^{-1}$. Raman analysis was performed with a Jobin Yvon HR800 Raman spectrometer. X-ray photoelectron spectroscopy (XPS) experiments were carried out on a VG scientific ESCALAB 2201XL instrument with the Al Kα X-ray radiation. The morphological characteristics of the samples were investigated by field emission scanning electron microscopy (FE-SEM; JEOL JSM-7500FA). Transmission electron microscope (TEM) images were collected on a JEOL 2011 200kV instrument.

5.2.3 Electrochemical measurements

The electrodes were prepared by mixing 80wt% as-prepared active materials with 10wt% carboxymethyl cellulose (CMC) binder dissolved in de-ionized water to form a homogeneousslurry. 10wt% Super P was also added. The electrode slurry was uniformly pasted onto copper foil and dried at 90° C. Electrochemical cells (CR2032) with the active materials as working electrode, Na foil as the counter electrode, a glass microfiber film as the separator, and 1M $NaClO_4$ dissolved in a 1:1 (v/v) mixture of ethylene carbonate (EC) and diethyl carbonate (DEC) with 5 wt% fluoroethylene carbonate (FEC) as the electrolyte were assembled in aglove box (H_2O, O_2<0.1 ppm, Mbraun, Ubilab, USA). Electrochemical impedance spectroscopy (EIS) and cyclic voltammetry (CV) were conducted on a VMP-3 electrochemical workstation at a scan rate of 0.1 mV s^{-1}.Galvanostatic charge/discharge was conducted using a LAND (CT2001A) battery tester over the voltage range of 0.001-2V versus Na/Na^+ at different constant current densities, which were based on the weight of the samples.

5.3 Results and discussion

5.3.1 Structure and morphology

X-ray diffraction (XRD) measurements were used to confirm the formation of SnS, and typical XRD patterns are presented in Fig. 5.2. The diffraction peaks of the XRD patterns for all the products prepared correspond to SnS. It can be seen that there are still some SnO_2 peaks in the resultant according to Figure 5.2. The subsequent compounds are compounds are a mixture of SnS and SnO_2. It is very difficult to make an identification of the graphene peaks and carbon peaks in the powder diffraction patterns due to the following reasons:

(1) The graphene content in the sample is quite low (about 10 wt%)

(2) The graphene sheets shows the features of disordered stacking, while the carbon also exhibits disorder.

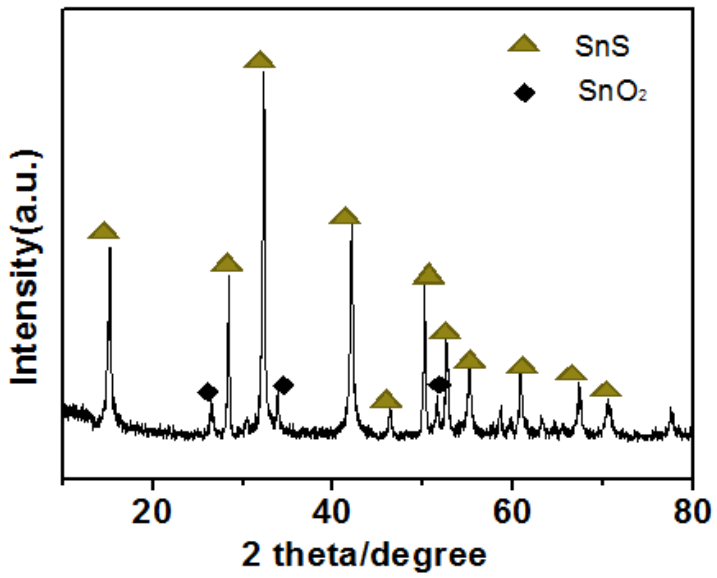

Figure 5.2 X-ray diffraction (XRD) patterns of subsequent compounds

Figure5.3 presents the Raman spectra of Gr-SnO_2-C and Gr-SnS-C. The peak at around 1575 cm^{-1} (G band) is related to the vibrations of sp^2-bonded carbon atoms in a 2-dimensional hexagonal lattice. In addition, the peak at 1341 cm^{-1} (D band) may be related to the defects and disorder in the hexagonal graphitic layers. The intensity ratio of the D-band to the G-band of SnS-GO-C was a bit higher than the ratio for SnO_2-GO-C, which indicates a reduction in the average size of the sp^2 domains after sulphidation. The enhancement could be due to several reasons, such as the amorphous carbon coating, the presence of SnS nanoparticles which were loaded on the graphene sheets, and the exfoliation of the GO.

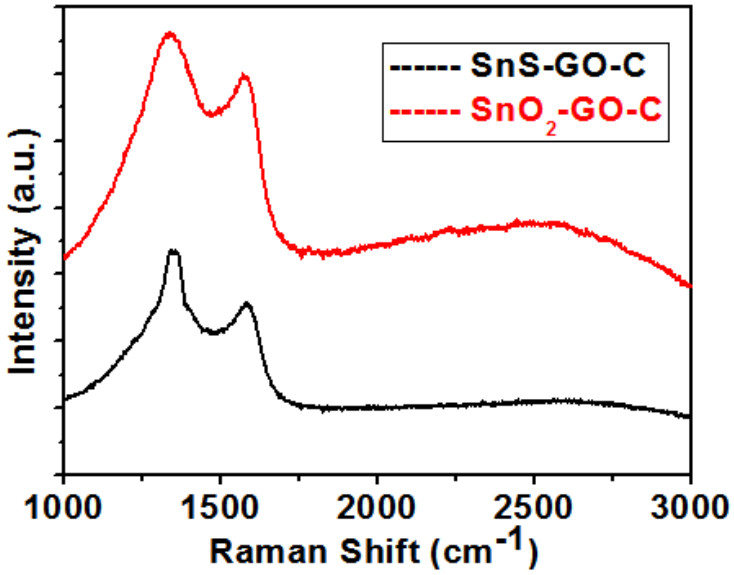

Figure 5.3 Raman spectra of Gr-SnO_2-C and Gr-SnS-C.

Typical scanning electron microscope (SEM) images of Gr-SnS-C and Gr-SnO_2-C are shown in Fig.5.4. It can be seen that both Gr-SnS-C and Gr-SnO_2-C have unique morphology. The nanoparticles are uniformly distributed on the graphene sheets. The average diameter of the large, thin sheets is approximately several hundred nanometers. Furthermore, the high resolution TEM image [Figure 5.4(e)] clearly exhibits a lattice spacing of 0.29nm. This corresponds well with the (101) planes of orthorhombic SnS.

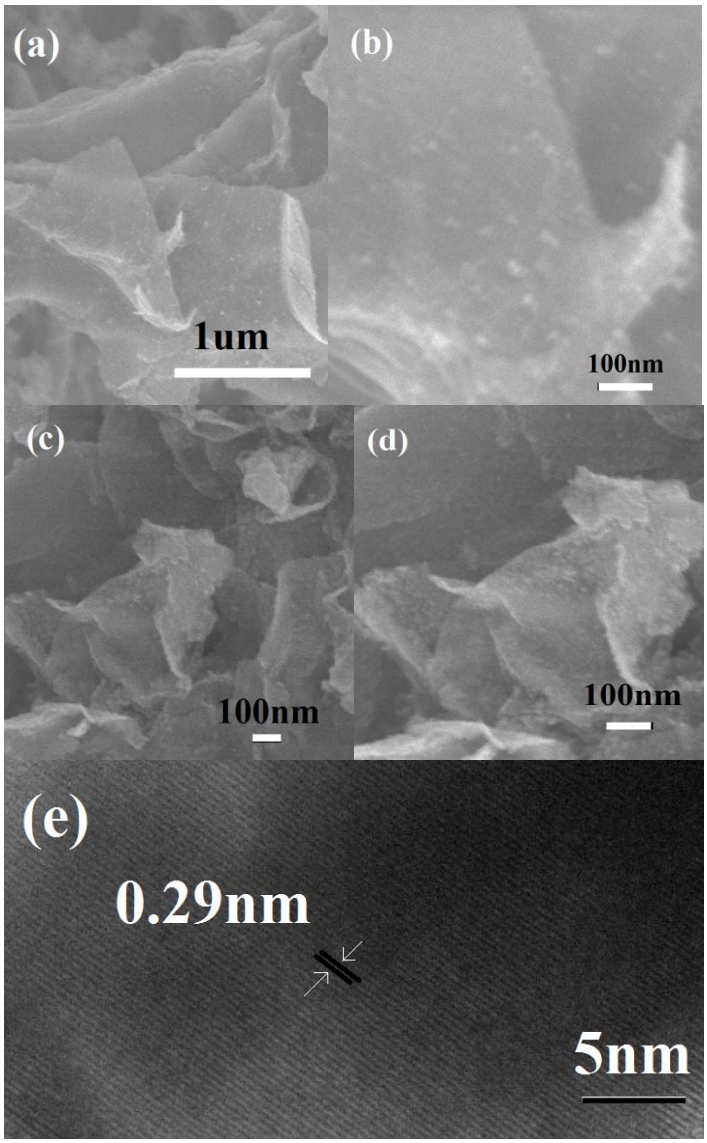

Figure 5.4 Low (a) and high (b) magnification SEM images of Gr-SnO_2-C composite; low (c) and high (d) magnification SEM images of Gr-SnS-C composite. (e) HRTEM image of the SnS-GO-C composite.

5.3.2 Electrochemical characterization

The electrochemical behaviour of the composites was initially characterized by cyclic

voltammery (CV). The curves are very similar to what has been reported. According to the literature, a peak occurs at about 1.1V that could be attributed to the formation of a solid electrolyte interphase (SEI) layer. In addition, a broad peak at around 0.6V could be due to the conversion and alloying reactions at a scanning rate of 0.1mV s^{-1} in the potential range of 0.001-1.0V. The basic reversible reactions of the composites during the charge and discharge processes are shown in Equations (5.1) and (5.2). The formula for the formation of SnS is shown in Equation (5.3).

$$\mathbf{SnS + 2Na^{+} + 2e^{-} \leftrightarrow Na_2S + Sn} \quad \textbf{(5.1)}$$

$$\mathbf{4Sn + 15Na^{+} + 15e^{-} \leftrightarrow Na_{15}Sn_4} \quad \textbf{(5.2)}$$

$$\mathbf{SnO_2 + Thiourea + H_2 \rightarrow SnS + H_2S + H_2 + H_2O} \quad \textbf{(5.3)}$$

With the operating voltage ranging from 0.01V to 2.5V, the initial discharge (sodiation) capacity was 904.7mAh g^{-1} at a current density of 30mA g^{-1}. The irreversible capacity loss in the initial cycle was about 300mAh g^{-1}, mainly due to the formation of SEI films, and the corresponding coulombic efficiency was 67.3%, as shown in Figure 5.5(a). Figure 5.5(b) presents the cycling performance of the Gr-SnS-C composite and Gr-SnO_2-C composite electrodes at a current density of 30mA g^{-1}. The Gr-SnS-C electrode delivered a discharge capacity of 673.1mAh g^{-1} after 70 cycles with approximately 100% coulombic efficiency. For comparison, the Gr-SnO_2-C electrode also provided a capacity of 533.2mAh g^{-1} after 70 cycles, which represented excellent cycling performance. The capacity retention of the Gr-SnO_2-C electrode was about 98.2%.

To further confirm the electrochemical performance of the Gr-SnS-C composite for SIB applications, the rate capability, which is regarded as an important performance indicator for grid-scale electricity storage and electric vehicle applications, was also investigated. The results are shown in Figure 5.5(c). The current density began at 30mA g^{-1} and was increased to 7290mA g^{-1} step by step. When the current density was 30mA g^{-1}, the reversible capacity

of the the Gr-SnS-C and Gr-SnO_2-C was 645mAh g^{-1} and 580mAh g^{-1} respectively. What is more, as the current density increased to 7290mA g^{-1}, the Gr-SnS-C composite still provided a capacity of nearly 300mAh g^{-1}, which represents excellent rate performance. The good rate performance may be due to its unique structure. The porous yolk-shell structure may reduce the diffusion of sodium ions, which leads to better capability for sodium ion insertion. The large volume between both the shell and the core and the carbon layer and the graphene layer also can easily allow the electrolyte into the microspheres, which can improve the performance of the Gr-SnS-C composite.

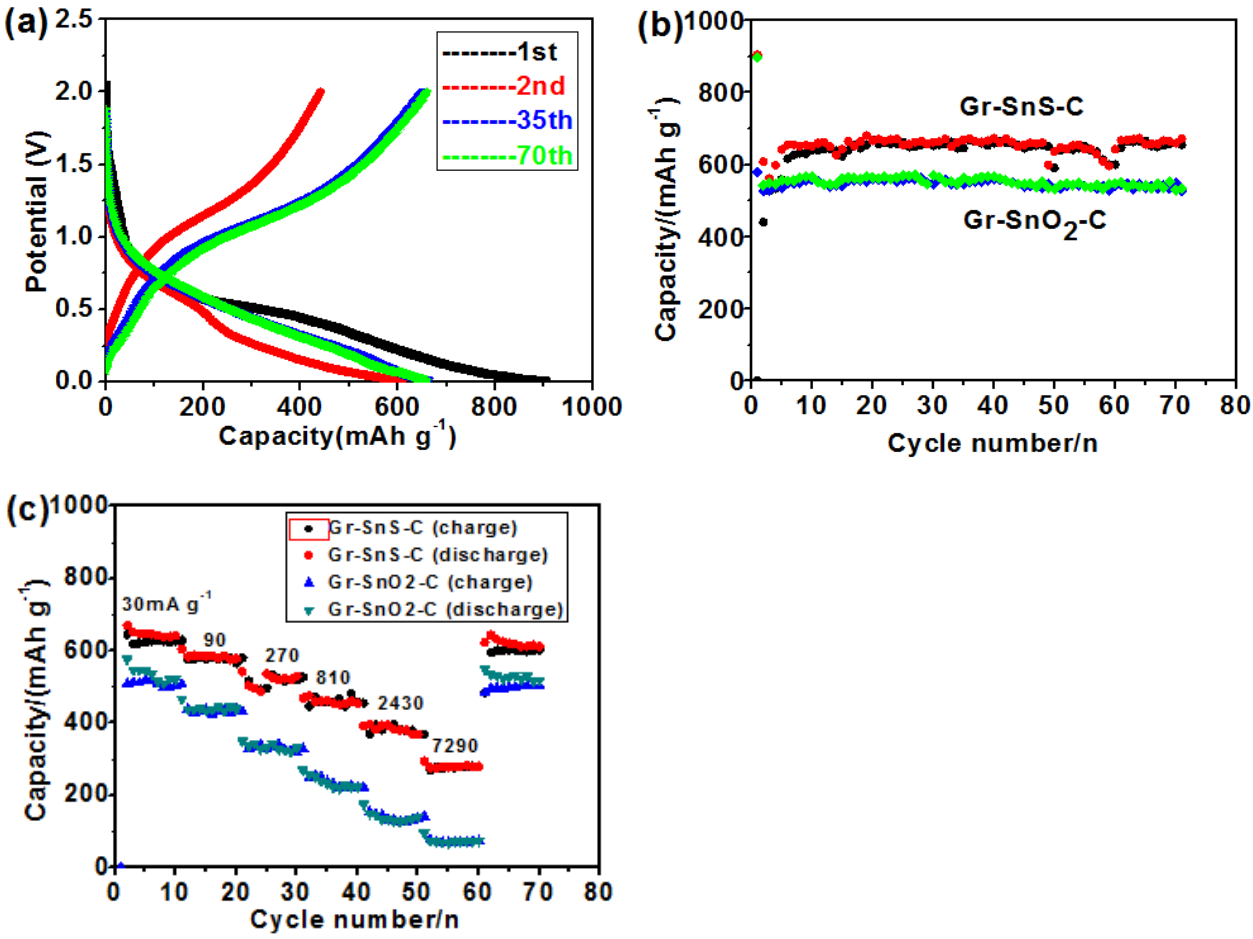

Figure 5.5 (a) Galvanostatic discharge-charge profiles for Gr-SnS-C electrode at a current density of 30 mA g^{-1}. (b) Comparisons of Gr-SnS-C electrode and Gr-SnO_2-C electrode for cyclic performance. (c) Comparisons of Gr-SnS-C electrode and Gr-SnO_2-C electrode for rate performance.

5.4 Conclusions

Gr-SnS-C material was prepared by an environmentally friendly hydrothermal method and a simple heat-treatment process. It includes carbon layers and graphene layers, which can endure the large volume changes during the charging and discharging processes. When tested in sodium-ion batteries, the Gr-SnS-C electrode presented dramatically improved, excellent cyclic stability and rate performance compared with the recently reported graphene@SnS composite.[88]Furthermore, Gr-SnS-C electrode also exhibits higher capacity and rate stability than the Gr-SnO_2-C electrode. Even at high current density, the Gr-SnS-C electrode still shows superior electrochemical properties, which may due to its unique structure. The graphene layer and the carbon coating layer can most importantly buffer the large volume changes, which make the structure totally stable. What is more, the yolk-shell structure not only has the function of preventing the diffusion of sodium ions which leads to the good conductivity, but also has the same function as the graphene and carbon coating layers.

In general, the Gr-SnS-C material synthesized by the two-step method seems to be a promising material which can be used in various applications, such as the gas sensors, nanoreactors, solar cells, etc. Furthermore, more carbon coated metal sulphides which are synthesized by the same method can be investigated due to the very interesting structure.

CHAPTER 6 CONCLUSIONS

All the investigations on electrode materials for sodium-ion batteries have been discussed above. Basically, the core part of the work is to design advantageous structures and morphologies by using various methods to enhance the electrochemical performance for practical applications of SIBs. In brief, synthesis of nanostructures and conductive additives normally have the following merits: reduction of the diffusion length of ions and electrons to short pathways, high surface area to increase the amount of reactive sites and electrode-electrolyte interface, conductivity improvement, and alleviation of structural variation. Therefore, in this thesis, the electrochemical properties of tin-antimony alloy nanocomposites and carbon-coated graphene@tin sulfide as alternative anode materials for sodium ion batteries have been investigated.

For the SnSb alloy composites, a series of similar materials have been synthesized for systematic research. For example, pure Sn, pure Sb, etc. were synthesized as reference samples to confirm the improvement of electrochemical performance for the alloy system. In addition, the selection of electrolyte was also investigated. There are three different common types of electrolyte that were used in the work. Through comparison, the best electrolyte was selected, which could then be used in the following step for intensive research. At the same time, two different solutions, of PVP and PAN, were also investigated to select the right one for better electrochemical performance. Finally, under all the best conditions, the SnSb alloy composite exhibits the best electrochemical performance, which suggests that it may be a promising material in the future.

For the Gr-SnS-C, the design is normally based on what has been recently reported, due to its many benefits mentioned above. The process can be demonstrated as a two-step method, which is very simple and environmentally friendly. The results show that both the Gr-SnS-C

material and the Gr-SnO_2-C exhibit excellent rate capability, even under very high current density, although the Gr-SnS-C presents a higher capacity (nearly 650mAh g^{-1}) than the Gr-SnO_2-C (580mAh g^{-1}) due to its unique structure. The yolk-shell structure can tolerate the large volume changes during the charging and discharging processes. The excellent cycling performance and rate performance means that this material can be used in various applications, such as sensors, solar cells, etc. Therefore, this material will be regarded as a promising material in the future.

Reference

[1] Winter M, Brodd RJ, *Chem Rev*, 2005, **104**,4245.

[2] S. W. Kim, D. H. Seo, X. H. Ma, G. Ceder, K. Kang, *Adv. Energy Mater*.,2012, **2**, 710.

[3] V. Palomares, P. Serras, I. Villaluenga, K. B. Hueso , J. C. Gonzalez, T. Rojo, *Energy Environ. Sci*., 2012, **5**, 5884.

[4] M. D. Slater, D. Kim, E. Lee, C. S. Johnson, *Adv. Funct. Mater*., 2013, **23**, 947.

[5] H. L. Pan, Y. S. Hu, L. Q. Chen, *Energy Environ. Sci*., 2013, **6**, 2338.

[6] Y. H. Lu, L. Wang, J. G. Cheng, J. B. Goodenough, *Chem. Commun*., 2012, **48**, 6544.

[7] S. P. Ong, V. L. Chevrier, G. Hautier, A. Jain, C. Moore, S. Kim, X. H. Ma, G. Ceder, *Energy Environ. Sci*., 2011, **4**, 3680.

[8] Tarascon JM, Armand M, *Nature*, 2001, **414**, 359.

[9]A. Yoshino, *Angew. Chem., Int. Ed.*, 2012, **51**, 5798.

[10] H. B. Wu, J. S. Chen, H. H. Hng, X. W. Lou, *Nanoscale*, 2012, **4**, 2526.

[11] J. M. Tarascon, M. Armand, *Nature*, 2001, **414**, 359.

[12] L. Hui, W. Chuan, W. Feng, B. Ying, *Acta Chim Sinica*, 2014, **72**, 21-29.

[13] Y. H. Sung, Y. J. Kim, Y. W. Park, *Energy Environ Sci*., 2013, **6**, 2067.

[14] C. Delmas, J. J. Braconnier, C. Fouassier, P. Hagenmuller, *Solid State Ionics*, 1981, **165**,3-4.

[15] L. W. Schacklette, T. R. Jew, L. Townsend, *J. Electrochem. Soc*., 1988, **135**, 2669.

[16] N. Yabuuchi, M. Kajiyama, J. Iwatate, H. Nishikawa, S. Hitomi, R. Okuyama, R. Usui, Y. Yamada, S. Komaba. *Nat. Mater*., 2012, **11**, 512.

[17] H. M. Liu, H. S. Zhou, L. P. Chen, Z. F. Tang, W. S. Yang, *J. Power Sources*. 2011, **13**, 938.

[18]B. L. Ellis, K. T. Lee and L. F. Nazar, *Chem. Mater.*, 2010, **22**, 691.

[19] J. J. Ding, Y. N. Zhou, Q. Sun, Z. W. Fu, *Electrochem. Commun*., 2012, **22**, 85.

[20] J. J. Wang and X. L. Sun, *Energy Environ. Sci.*, 2012, **5**, 5163.

[21] N. Anantharamulu, K. K. Rao, G. Rambabu, *J. Mater. Sci*., 2011, **46**, 4821.

[22] K. Du, H. W. Guo, G. R. Hu, Z. D. Peng, Y. B. Cao, *J. Power Sources*, 2013, **223**, 284.

[23] Z. L. Jian, L. Zhao, H. L. Pan, Y. S. Hu, H. Li, W. Chen, L. Q. Chen, *Electrochem. Commun*., 2012, **14**, 84.

[24] B. L. Ellis, W. R. M. Makahnouk, Y. Makimura, K. Toghill, L. F. Nazar, *Nat. Mater*., 2007, **6**, 749.

[25] A. Langrock, Y. H. Xu, Y. H. Liu, S. Ehrman, A. Manivannan, C. S. Wang, *J. Power Sources*, 2013, **223**, 62.

[26] N. Recham, J. N. Chotard, L. Dupont, K. Djellab, M. Armand, J. M. Tarascon, *J. Electrochem. Soc*., 2009, **156**, A993.

[27] V. Palonares, P. Serras, I. IVillaluenga, *Energy Environ. Sci.*, 2011, **3**, 5884.

[28] K. Chihara, A. Kitajou, D. Gocheva, S. Okada, J.I. Yamaki, *J. Power Sources*, 2013, **227**, 80.

[29] I. D. Gocheva, M. Nishijima, T. Doia, S. Okada, J. Yamaki, *J Power Sources*, 2009, **187**, 247.

[30] M. Nishijima, I. D. Gocheva, S. Okada, T.Doia, J Yamakia, T. J. Nishida, *J Power Sources*, 2009, **190**, 558.

[31] A. Kitajou, H. Komatsu, K. Chihara, I. D. Gocheva, S. Okada, J. Yamaki, *J Power Sources*, 2009, **198**, 389.

[32] A. Yamada, S. C. Chung, K. Hinokuma, J. *Electrochem. Soc*., 2001, **148**, 224.

[33] T. Nagaura, K. Tozawa, *Batteries Solar Cells*, 1990, **9**, 209.

[34] P. Ge, M. Fouletier, *Solid State Ionics*, 1998, **28**, 1172.

[35] D. A. Stevens, J. R. Dahn, *J. Electrochem. Soc*., 2001, **148**, 803.

[36] V. L. Chevrier, G. Ceder, *J. Electrochem. Soc*., 2011, **158(9)**, A1011.

[37] R.Alcantara, J. M. Jim, P. Lavela, J. L. Tirado, *Electrochem. Commun.*, 2001, **3(11)**, 639.

[38] S. Komaba, W. Murata, T. Ishikawa, N. Yabuuchi, T. Ozeki, T. Nakayama, A. Ogata, K. Gotoh, K.Fujiwara, *Adv. Funct. Mater*., 2011, **21**, 3859.

[39] K. Tang, L. J. Fu, R. J. White, L. H. Yu, M. M. Titirici, M. Antonietti, J. Maier, *Adv. Eng. Mater*., 2012, **2**, 873.

[40] Y. L. Cao, L. F. Xiao, M. L. Sushko, W. Wang, B. Schewenzer, J. Xiao, Z. M. Nie, L. V. Saraf, Z. G. Yang, J. Liu, *Nano lett.*, 2012, **12**, 3783.

[41] K. Gotoh, T. Ishikawa, S. Shimadzu, N. Yabuuchi, S. Komaba, K. Takeda, A. Goto, K. Deguchi, S. Ohki, K. Hashi, T. Shimizu, H. J. Ishida, *J. Power Sources*, 2013, **225**, 137.

[42] B. L. Ellis, L. F. Nazar, *Solid State Mater. Sci.*, 2012, **16**, 168.

[43] J. Yang, M. Winter, J. O. Besenhard, *Solid State Ionics*, 1996, **90**, 281.

[44] C. M. Park, H. J. Sohn, *Electrochim, Acta*, 2009, **54**, 6367.

[45] C. M. Park, K. J. Jeon, *Chem. Commun*., 2011, **47**, 2122.

[46] J. Hassoun, G. Derrien, S. Panero, B. Scrosati, Electrochim. Acta, 2009, **54**, 4441.

[47] U. Kasavajjula, C. Wang, J. Appleby, *J. Power Sources*, 2007, **163**, 1003.

[48] M. K. Datta, R. Epur, P. Saha, K. Kadakia, S. K. Park, P. N. Kumta, *J Power Sources*, 2013, **225**, 316-322.

[49] Y. Xu, Y. Zhu, Y. Liu, C. Wang, *Adv. Energy Mater*., 2013, **3**, 128-133.

[50] H. Zhu, Z. Jia, Y. Chen, N. J. Weadock, J. Wan, O. vaaland, X. Han, T. Li, L. Hu, *Nano Lett.*, 2013, **13**, 3093-3100.

[51] J. Qian, Y. Chen, L. Wu, Y. Cao, X. Ai, H. Yang, *Chem. Commun.*, 2012, **48**, 7070-7072.

[52] A. Darwiche, C. Marino, M. T. Sougrati, B. Fraisse, L. Stievano, L. Monconduit, *J. Am. Chem. Soc.*, 2012, **134**, 20805-20811.

[53] A. Darwiche, M. T. Sougrati, B. Fraisse, L. Stievano, L. Monconduit, *Electrochem. Commun.*, 2013, **32**, 18-21.

[54] L. Xiao, Y. Cao, J. Xiao, W. Wang, L. Kovarik, Z. Nie, J. Liu, *Chem. Commun.*, 2012, **48**, 3321-3323.

[55] L. W. Ji, M. Gu, Y. Y. Shao, X. L. Li, H. E. Mark, W. A. Bruce, W. Wang, Z. M. Nie, J. Xiao, C. M. Wang, J. G. Zhang, J. Liu, *Adv. Mater.*, 2014, **26**, 2901-2908.

[56] L. Baggetto, E. Allcorn, A. Manthiram, G. M. Veithm, *Electrochem. Commun.*, 2013, **27**, 168.

[57] J. F. Qian, Y. Chen, L.Wu, Y. L. Cao, X. P. Ai, H. X. Yang, *Chem. Commun.*, 2012, **48**, 7070.

[58] L. Wu, F. Pei, R. Mao, F. Y. Wu, J. F. Qian, Y. L. Cao, X. P. Ai, H. X. Yang, *Electrochim. Acta*, 2013, **87**, 41.

[59] L. F. Xiao, Y. L. Cao, J. Xiao, W. Wang, L. Kovarik, Z. M. Nie, J. Liu, *Chem. Commun.*, 2012, **48**, 3321.

[60] Z. Chen, V. Chevier, L. Christensen, J. R. Dahn, *Electrochem. Solid-State. Lett.*, 2004, **7**, 310.

[61] W. R. Liu, M. H. Yang, H. C. Wu, S. M. Chiao, N. L. Wu, *Electrochem. Solid-State. Lett.*, 2005, **8**, 100.

[62] Z. Chen, L. Christensen, J. R. Dahn, *Electrochem. Commun.*, 2003, **5**, 919.

[63] B. Lestriez, S. Bahri, I. Sandu, L. Roue, D. Guyomard, *Electrochem. Commun.*, 2007, **9**, 2801.

[64] N. S. Hochgatterer, M. R. Schweiger, S. Koller, P. R. Raimann, T. Wohrle, C. Wurm, M. Wintet, *Electrochem. Solid-State. Lett.*, 2008, **11**, 76.

[65] L. Chen, X. Xie, J. Xie, K. Wang, J. Wang, *J. Appl. Electrochem.*, 2006, **36**, 1099.

[66] H. P. Klug and L. E. Alexander, *X-ray Diffraction Procedure for Polycrystalline and Amorphous Materials*, Wiley, New York, 1974.

[67] Z. Yang, J. Zhang, M. C. W. Kintner-Meyer , X. Lu , D. Choi , J. P. Lemmon , J. Liu , *Chem. Rev.*, 2011 , **111** , 3577 – 3613.

[68] J. Liu, J.-G. Zhang, Z. Yang, J. P. Lemmon, C. Imhoff, G. L. Graff, L. Li, J. Hu, C. Wang , J. Xiao, G. Xia, V. V. Viswanathan, S. Baskaran, V. Sprenkle, X. Li, Y. Shao, B. Schwenzer, *Adv. Funct. Mater.*, 2012, **23**, 929-946.

[69] B. L. Ellis, L. F. Nazar, Curr. Opin. *Solid State Mater. Sci.*, 2012, **16**, 168 – 177.

[70] S.-W. Kim, D.-H. Seo, X. Ma, G. Ceder, K. Kang, *Adv. Energy Mater.*, 2012, **2**, 710 – 721.

[71] S. Komaba, W. Murata, T. Ishikawa, N. Yabuuchi, T. Ozeki, T. Nakayama, A. Ogata, K. Gotoh, K. Fujiwara, *Adv. Funct. Mater.*, 2011, **21**, 3859 –3867.

[72] M. D. Slater, D. Kim, E. Lee, C. S. Johnson, **Adv. Funct. Mater.**, 2012, **23**, 947 – 956.

[73] N.-S. Choi, Z. Chen, S. A. Freunberger, X. Ji, Y. K. Sun, K. Amine, G. Yushin, L. F. Nazar, J. Cho, P. G. Bruce, *Angew. Chem.*, 2012, **51**, 9994 – 10024.

[74] Y.-U. Park, D.-H. Seo, H.-S. Kwon, B. Kim, J. Kim, H. Kim, I. Kim, H. I. Yoo, K. Kang, *J. Am. Chem. Soc.*, 2013, **135**, 13870 – 13878.

[75] H. Pan, Y. S. Hu, L. Chen, *Energy Environ. Sci.*, 2013, **6**, 2338 – 2360.

[76] N. Yabuuchi, M. Kajiyama, J. Iwatate, H. Nishikawa, S. Hitomi, R. Okuyama, R. Usui, Y. Yamada, S. Komaba, *Nat. Mater.*, 2012, **11**, 512 – 517.

[77] Y. Cao, L. Xiao, W. Wang, D. Choi, Z. Nie, J. Yu, L. V. Saraf, Z. Yang, J. Liu, *Adv. Mater.*, 2011, **23**, 3155 – 3160.

[78] Z. Jian, L. Zhao, H. Pan, Y. S. Hu, H. Li, W. Chen, L. Chen, *Electrochem. Commun.*, 2012, **14**, 86 – 89.

[79] Z. Jian, W. Han, X. Lu, H. Yang, Y. S. Hu, J. Zhou, Z. Zhou, J. Li, W. Chen, D. Chen, L. Chen, *Adv. Energy Mater.*, 2013, **3**, 156 – 160.

[80] L. Zhao, J. Zhao, Y. S. Hu, H. Li, Z. Zhou, M. Armand, L. Chen, *Adv. Energy Mater.*, 2012, **2**, 962 – 965.

[81] Q. Ru, S. J. Hu, Z. W. Zhang, W. Peng, X. H. Hou, Z. W. Huang, *Chin. Sci. Bull*, 2011, **55**, 3113.

[82] S. C. Zhang, Y. L. Xing, T. Jiang, Z. J. Du, F. Li, L. He, W. B. Liu, *J. Power Sources*, 2011, **196**, 6915.

[83] C. G. Yang, D. W. Zhang, Y. B. Zhao, Y. H. Lu, L. Wang, J. B. Goodenough, *J. Power Sources*, 2011, **196**, 10673.

[84] R. M. Gnanamuthu, S. Mohan, C, W, Lee, *Mater. Lett.*, 2012, **84**, 101.

[85] J. O. Bensenhard, J. Yang, M. Winter, *J. Power Sources*, 1997, **68**, 87.

[86] J. Yang, Y. Takeda, N. Imanishi, O. Yamamoto, *J. Electrochem. Soc.*, 1999, **146**, 4009.

[87] F. J. Fernandez-Madrigal, P. Lavela, C. P. Vicente, J. L. Tirado, *Chem. Mater.*, 2002, **14**, 2962.

[88] J. Hassoun, G. Derrien, S. Panero, B. Scrosati, *J. Power Sources*, 2008, **183**, 339.

[89] M. Morcrette, D. Larcher, J. M. Tarascon, K. Edstrom, J. T. Vaughey, M. M. Thackeray, *Electrochim. Atca*, 2007, **52**, 5339.

[90] X. H. Lu, W. X. Zhao, G. R. Li, H. E. Hong, Y. X. Tong, *Mater. Lett.*, 2008, **62**, 4280.

[91] Y. X. Zheng, J. Xie, S. Y. Liu, W. T. Song, G. S. Cao, T. J. Zhu, X. B. Zhao, *J. Power Sources*, 2012, **202**, 276.

[92] K. Xu, A. von Cresce, *J. Mater. Chem.*, 2011, **21**, 9849 – 9864.

[93] K. Amine, I. Belharouak, Z. Chen, T. Tran, H. Yumoto, N. Ota, S. T. Myung, Y. K. Sun, *Adv. Mater.*, 2010, **22**, 3052 – 3057.

[94] S. W. Lee, B. M. Gallant, H. R. Byon, P. T. Hammond, Y. Shao-Horn, *Energy Environ. Sci.*, 2011, **4**, 1972 – 1985.

[95] J. Shu, H. Li, R. Yang, Y. Shi, X. Huang, *Electrochem. Commun.*, 2006, **8**, 51 – 54.

[96] C. K. Chan, R. Ruffo, S. S. Hong, Y. Cui, *J. Power Sources*, 2009, **189**, 1132 – 1140.

[97] H. Nakai, T. Kubota, A. Kita, A. Kawashima, *J. Electrochem. Soc.*, 2011, **158**, A798 – A801.

[98] V. Etacheri, O. Haik, Y. Goffer, G. A. Roberts, I. C. Stefan, R. Fasching, D. Aurbach, *Langmuir*, 2011, **28**, 965 – 976.

[99] M. Herstedt, A. M. Andersson, H. Rensmo, H. Siegbahn, K. Edström, *Electrochim. Acta*, 2004, **49**, 4939 – 4947.

[100] J. T. Lee, N. Nitta, J. Benson, A. Magasinski, T. F. Fuller, G. Yushin, *Carbon*, 2013, **52**, 388 – 397.

[101] X. W. Lou, Y. Wang, C. L. Yuan, Z. Y. Jiang, D. Y. Zhao, *Adv. Mater.*, 2004, **16**, 1432-6.

[102] Y. L. Zhang, Y. Liu, M. L. Liu, *Chem. Mater.*, 2006, **18**, 17832-7.

[103] Y. Wang, J. Y. Lee, *J. Phys. Chem. B.*, 2004, **18**, 4643-6.

[104] S. J. Han, B. C. Jang, T. Kim, S. M. Oh, T. Hyeon, *Adv. Funct. Mater.*, 2005, **15**, 1845.

[105] Y. Wang, J. Y. Lee, H. C. Zeng, *Chem. Mater.*, 2005, **17**, 3899.

[106] D. Deng, J. Y. Lee, *Chem. Mater.*, 2008, **20**, 1841.

[107] Y. Cao, L. Xiao, W. Wang, D. Choi, Z. Nie, J. Yu, L. V. Saraf, Z. Yang, J. Liu, *Adv. Mater.*, 2011, **23**, 3155.

[108] L. G. Xue, X. Xia, T. Tucker, K. Fu, S. Zhang, S. L. Li, X. W. Zhang, *J. Mater. Chem. A.*, 2013, **1**, 13807-13813.

[109] L. Xue, G. Xu, Y. Li, S. Li, K. Fu, Q. Shi and X. Zhang, *ACS Appl. Mater. Interfaces*, 2013, **5**, 21–25.

[110] L. Ji, Z. Lin, A. J. Medford and X. Zhang, *Carbon*, 2009, **47**, 3219–3226.

[111] L. Xue, K. Fu, Y. Li, G. Xu, Y. Lu, S. Zhang, O. Toprakci and X. Zhang, *Nano Energy*, 2013, **2**, 361–367.

[112] C. Kim, K. Yang, M. Kojima, K. Yoshida, Y. Kim, Y. Kim and M. Endo, *Adv. Funct. Mater.*, 2006, **16**, 2393–2397.

[113] N. Liu, L. Hu, M. T. McDowell, A. Jackson and Y. Cui, *ACS Nano*, 2011, **5**, 6487.

[114] Q. M. Pan, H. B. Wang and Y. H. Jiang, *Electrochem. Commun.*, 2007, **9**, 754–760.

[115] D. Aurbach, I. Weissman, A. Schechter, H. Cohen, *Langmuir*, 1996, **12**, 3991 – 4007 ;

[116] Y.-C. Chiang, C.-Y. Lee, H.-C. Lee, *Mater. Chem. Phys.*, 2007, **101**, 199 – 210

[117] G. Beamson, D. Briggs, *High Resolution XPS of Organic Polymers: The Scienta ESCA300 Database*, 1992 , **295**pp.

[118] M. Zhang, D. Lei, Z. Du, X. Yin, L. Chen, Q. Li, *J Mater. Chem.*, 2011, **114**, 21770.

[119] O. Akhavan, *ACS Nano*, 2010, **4**, 4174.

[120] X. Xia, J. R. Dahn, *J. Electrochem. Soc.*, 2012, **159**, A515 – A519.

[121] L. D. Ellis, T. D. Hatchard, M. N. Obrovac, *J. Electrochem. Soc.*, 2012, **159**, A1801 – A1805.

[122] S. Komaba, T. Ishikawa, N. Yabuuchi, W. Murata, A. Ito , Y. Ohsawa, *ACS Appl. Mater. Interfaces*, 2011, **3**, 4165 – 4168.

[123] L. Ji, Z. Lin, A. J. Medford, X. Zhang, *Chem. Eur. J.* , 2009, **15**, 10718 – 10722.

[124] L. Ji, Z. Lin, B. Guo, A. J. Medford, X. Zhang, *Chem. Eur. J.*, 2010, **16**, 11543 – 11548.

[125] X. Zhang, L. Ji, O. Toprakci, Y. Liang, M. Alcoutlabi, *Polym. Rev.*, 2011, **51**, 239 – 264.

[126] L. Ji, Z. Lin, M. Alcoutlabi, X. Zhang, *Energy Environ. Sci.*, 2011, **4**, 2682 – 2699.

[127] M. Armand, J. M. Tarascon, *Nature*, 2008, **451**, 652-7.

[128] S. M. Peak, E. Yoo, I. Honma, *Nano lett.*, 2009, **9**, 72-5.

[129] Z. Yang, J. Zhang, M. C. W. Kinter-Meyer, X. Lu, D. Choi, J. P. Lemmon, J. Liu, *Chem. Rev.*, 2011, **111**, 3577.

[130] C. Wadia, P. Albertus, V. Srinivasan, *J. Power Sources*, 2011, **196**, 1593.

[131] S. P. Ong, V. L. Chevrier, G. Hautier, A. Jain, C. Moore, S. Kim, X. Ma, G. Ceder, *Energy Environ. Sci.*, 2011, **4**, 3680.

[132] D. Kim, E. Lee, M. Slater, W. Lu, S. Rood, C. S. Johnson, *Electrochem. Commun.*, 2012.

[133] M. M. Doeff, Y. Ma, S. J. Visco, L. C. De Jonghe, *J. Elctrochem. Soc*., 1993, **140**, L169.

[134] E. Zhecheva, R.Stoyanova, J. M. Jimenez-Mateos, R. Alcantara, P. Lavela, J. L. Tirado, *Carbon*, 2002, **40**, 2301.

[135] R. Alcantara, J. M. Jimenez-Mateos, P. Lavela, J. L. Tirado, *Electrochem. Commun.*, 2001, **3**, 639.

[136] J. Akridge, R. Brodd, Pacific Power Symposium, Waikoloa, *Hawaii*, **2010**.

[137] "Market," The Lithium Site, 2012, http:// www.lithiumsite.com/ market.html. (Accessed February 2012).

[138] I. Exnar, J. Hep, *J. Power Sources*, 1993, **44**, 701.

[139] R. J. Jasinski, *Electroanal. Chem.*, 1970, **26**, 189.

[140] X. L. Zhou, T. F. Zhou, J. C. Hu, J. L. Li, *CrystEngComm*., 2012, **14**, 5627.

[141] P. Han, H. Wang, Z. Liu, X. Chen, L. A. Archer, *Chem. Mater*., 2009, **21**, 2868-74.

[142] H. Kim, D. H. Seo, S. W. Kim, J. Kim, K. Kang, *Carbon*, 2011, **49**, 326-32.

[143] X. Wang, X. Zhou, K. Yao, J. Zhang, Z. Liu, *Carbon*, 2011, **49**, 133-9.

[144] H. Xiang, K. Zhang, G. Ji, J. Y. Lee, C. Zou, X. Chen, *Carbon*, 2011, **49**, 1787-96.

[145] M. Zhang, D. Lei, Z. Du, X. Yin, L. Chen, Q. Li, *J. Mater. Chem.*, 2011, **21**, 1673.

[146] G. Wang, X. Shen, J. Yao, J. Park, *Carbon*, 2009, **47**, 2049-53.

[147] Y. M. Li, X. J. Lv, J. Lu, J. H. Li, *J. Phys. Chem. C.*, 2010, **114**, 21770.

[148] E. Yoo, J. Kim, E. Hosono, H. Zhou, T. Kudo, I. Homma, *Nano lett.*, 2008, **8**, 2277-82.

[149] C. F. Zhang, X. Peng, Z. P. Guo, C. B. Cai, Z. X. Chen, D. Wexler, S. Li, H. K. Liu, *Carbon*, 2011, **12**, 40.

[150] X. W. Lou, L. A. Archer, Z. C. Yang, *Adv. Mater*., 2008, **20**, 3987.

[151] Y. Zhao, L. Jiang, *Adv. Mater*., 2009, **21**, 3621.

[152] W. Li, Y. H. Deng, Z. X. Wu, X. F. Qian, J. P. Yang, Y. Wang, D. Gu, F. Zhang, B. Tu, D. Y. Zhao, *J. Am. Chem. Soc.*, 2011, **13**3, 15830.

[153] W. Cho, Y. H. Lee, H. J. Lee, M. H. Oh, *Adv. Mater.*, 2011, **23**, 1720.

[154] J. Liu, S. Z. Qiao, J. S. Chen, X. W. Lou, X. R. Xing, G. Q. Lu, *Chem. Commun.*, 2011, **47**, 12578.

[155] I. K. Lee, J. B. Joo, Y. D. Yin, F. Zaera, *Angew. Chem. Int. Ed.*, 2011, **50**, 10208.

[156] J. G. Lee, J. C. Park, H. J. Song, *Adv. Mater.*, 2008, **20**, 1523.

[157] J. Liu, Y. C. Zhou, J. B. Wang, Y. Pan, D. F. Xue, *Chem. Commun.*, 2011, **47**, 10380.

[158] J. Liu, H. Xia, D. F. Xue, L. Lu, *J. Am. Chem. Soc.*, 2009, **131**, 1 2086.

[159] X. W. Lou, C. L. Yuan, L. A. Archer, *Small*, 2007, **3**, 261.

[160] N. Liu, H. Wu, M. T. McDowell, Y. Yao, C. M. Wang, Y. Cui, *Nano Lett.*, 2012, **12**, 3315.

[161] Z. Y. Wang, L. Zhou, X. W. Lou, *Adv. Mater.*, 2012, **24,** 1903.

[162] S. L. Xiong, H. C. Zeng, *Angew. Chem. Int. Ed.*, 2012, **51**, 949.

[163] Z. Fang, Y. F. Liu, X. W. Liu, Q. Wang, Y. T. Fan. W. Z. Wang, *Cryst.eng.Comm.*, 2011, **13**, 5653.